SACOMAR
Technologies for Safe and Controlled Martian Entry

SPA.2010.3.2-04

EU-Russia Cooperation for Strengthening Space Foundations (SICA)

Re-entry Technologies and Tools

Theme 9 - Space
Activity 9.3 - Cross-Cutting-Activities
Area 9.3.2 - International Cooperation

Deliverable Reference Number: D7.11
Deliverable Title: Numerical simulation of IPG-4 experiments in CO_2+N_2 flow

Due date of deliverable: 29th February 2012

Actual submission date: 20th March 2012

Start date of project: 20th January 2011

Duration: 18 months

Organization name of lead contractor for this deliverable: IPM

Revision 1: First version of the report

Project co-funded by the European Commission within the 7th Framework Programme		
Dissemination Level		
PU	Public	X
PP	Restricted to other programme participants (including the Commission Services)	
RE	Restricted to a group specified by the consortium (including the Commission Services)	
CO	Confidential, only for members of the consortium (including the Commission Services)	

APPROVAL

Title	**issue**	revision
Numerical simulation of IPG-4 experiments in CO_2+N_2 flow	1	1

Author(s)	**20-03-2012**
A. Kolesnikov, S. Vasilevskii, A. Gordeev, A. Levitin	

Approved by	**Date**
Deputy Director of IPM S. Surzhikov	**20-03-2012**

Table of Contents

List of figures

List of tables

Nomenclature

z, r	[m]	Axial and radial coordinates (problem formulations for Alpha and Beta codes)
u, v, w	[m/s]	Velocity components (problem formulations for Alpha and Beta

		codes)
P	[Pa]	Pressure
ρ	[kg/m^3]	Density
h	[MJ/kg]	Enthalpy
h_e	[MJ/kg]	Enthalpy at the boundary layer external edge in front of testing model
T	[K]	Temperature
C_i	-	Mass fraction of the i-th species
X_i	-	Molar fraction of the i-th species
J_i	[kg/(s·m^2)]	Mass diffusion flux of the i-th species
K_w	[m/s]	Catalytic recombination rate
m	[kg/kmol]	Molar mass of gas mixture
N_{ap}	[kW]	Anode power of RF-generator
N_{pl}	[kW]	Power input in plasma
q_w	[W/cm^2]	Stagnation point heat flux
R_A	[J/mol/K]	Universal gas constant
Re	-	Reynolds number
R_m	[m]	Radius of tested model
Zm	[m]	Distance from discharge channel exit to the model
γ_w	-	Catalytic efficiency of surface recombination reactions

Subscripts

0	Stagnation condition
e	External edge of boundary layer
w	Surface of testing model
c	Gas parameters at the channel exit section

Acronyms

CFD	Computational Fluid Dynamics
ICP	Inductively coupled plasma
IPG-4	RF-plasmatron of IPM, Moscow
IPM	Institute for Problems in Mechanics
TPM	Thermal protection material
TPS	Thermal protection system
RF	Radio-frequency
WP	Work Package
LTE	Local thermal and chemical equilibrium

1 Executive summary

1.1 Scope of the deliverable

- Numerical simulation of subsonic 97%CO_2+3%N_2 plasma flow in IPG-4 discharge channel by Alpha code for the test conditions realized by the IPG-4 plasmatron with the segmented channel and sonic cylindrical nozzle.

- Numerical simulation of 97%CO_2+3%N_2 subsonic equilibrium reacting jet flow over euromodel by Beta code for the four IPG-4 test regimes to provide the set of dimensionless parameters that are necessary as the input data for Gamma code.

- Numerical simulation of subsonic ICP flow in IPG-4 discharge channel (Alpha) and the equilibrium dissociated jet flow over euromodel (Beta) for pure CO_2 working gas to compare with the corresponding results for 97%CO_2+3%N_2 flow and estimate the influence of 3%N_2 addition to the gas mixture.

- Numerical simulations of 5-species (CO_2, O_2, CO, O, C) nonequilibrium boundary layer flow with finite thickness to determine heat flux envelopes for the test conditions realized by the IPG-4 facility with CO_2 working gas.

- Validation of the novel model of surface catalysis, and determination of recombination coefficients γ_{wO} and γ_{wCO} for stainless steel and quartz using the novel model of catalytic recombination of O-atoms and CO-molecules on surface.

1.2 Results

A. Subsonic ICP flow parameters in IPG-4 segmented discharge channel with conical nozzle are calculated by Alpha code on the basis of Navier-Stokes and simplified Maxwell equations for the four IPG-4 test regimes realized for 97%CO_2+3%N_2 working gas according test matrix.

B. Parameters of 97%CO_2+3%N_2 equilibrium reacting subsonic jet flow over euromodel are calculated by Beta code on the basis of Navier-Stokes equations for the same IPG-4 test conditions.

C. The complete set of the dimensionless parameters is determined by Beta code computation results to be used as input data for Gamma code. These parameters characterize the boundary layer thickness, flow velocity and vorticity at the external edge of boundary layer in front of the testing model.

D. Numerical simulations of both ICP flow in discharge channel and subsonic jet flow over euromodel are performed for pure CO_2 working gas to compare with corresponding results obtained for 97%CO_2+3%N_2 flow. Comparison of the results revealed negligible influence of 3%N_2 addition on the main flow parameters and molar concentrations at the boundary layer external edge in front of the model.

E. One-dimensional 5-species (CO_2, O_2, CO, O, C) flow in nonequilibrium dissociated boundary layer with finite thickness near the model stagnation point was calculated by Gamma code to determine heat flux envelopes for the IPG-4 test regimes with CO_2 working gas. The calculations were made for the standard and the novel model of surface catalysis for O-atoms and CO-molecules recombination proposed in [34].

F. Comparison of calculations performed by the standard and the novel model of surface catalysis for the case $\gamma_{wO} = \gamma_{wCO} = \gamma_w$ shows that heat flux values q_w (T_w, γ_w) calculated by the novel model (within its application limits) are always higher than corresponding values calculated by the standard model. Consequently, values of the efficient recombination coefficient γ_w obtained with the novel model will be lower.

G. Partial heat flux envelopes are calculated by the novel model with different recombination coefficients γ_{wO} and γ_{wCO}, when one of the two coefficients is fixed, while the other is variable. For this two-parameter case, measured heat flux value to a testing material could be reproduced by Gamma computations with different pairs of (γ_{wO}, γ_{wCO}). To determine the unique solution, one can specify a fixed value for γ_{wO}, e.g. with use of appropriate literature data.

H. CO recombination coefficients γ_{wCO} are determined by the novel model for quartz and stainless steel for the four test regimes with use of the following fixed values of γ_{wO} taken from [37], [38]: γ_{wO} =2e-3 for quartz and γ_{wO} =2.6e-3 for steel. Comparison of the effective recombination coefficient $\gamma_w = \gamma_{wO} = \gamma_{wCO}$ obtained previously [34] by the standard model with the newly obtained catalytic efficiencies γ_{wO} and γ_{wCO} is presented. Value of γ_{wCO} is always lower (or equal) than the corresponding fixed value of γ_{wO}; both γ_{wO} and γ_{wCO} are lower than the corresponding effective recombination coefficient γ_w. So, the effective parameter γ_w provides probably the upper bound for the surface recombination coefficients γ_{wO} and γ_{wCO}.

1.3 Specific highlights

CFD simulation of plasmas and reacting gas flows and heat transfer for the IPG-4 plasmatron subsonic test conditions is the indispensable part of investigation of the catalytic properties of testing materials. Specific feature of IPM approach is the use of 1-D Gamma code coupled with appropriate experimental measurements to determine effective recombination coefficients together with rebuilding free stream parameters in facility. CFD calculations ICP and reacting gas flow fields by Alpha and Beta codes provide the set of dimensionless parameters to be used as input data for Gamma code. These dimensionless parameters are conservative, i.e. they slightly depend on plasmatron test conditions (pressure and RF-generator power).

1.4 Forms of integration within the work package and with other WPs

D7.11 is directly connected with D5.4 and D6.4. Results obtained in D7.11 are necessary to calculate heat flux envelopes and to determine effective recombination coefficients γ_{wO} and γ_{wCO} at the surface of testing materials that should be one of valuable results of the SACOMAR Project.

1.5 Problem areas

Numerical simulation revealed the limitation on the use of the novel model: input data for calculation (e.g. pressure, enthalpy, recombination coefficients) have to ensure sufficient concentration of oxygen atoms C_O in gas flow at the wall to provide the possibility of surface recombination for CO molecules defined by the corresponding recombination efficiency γ_{wCO}. When this condition is not provided, negative values of C_O appear in boundary layer computation to manifest inapplicability of the novel model for current regime and computation parameters (T_w, γ_w).

2 Introduction

Inductively coupled plasma flow is one of the important objects of numerical simulation from viewpoint of different applications and studying physical processes. A modern direction of the

induction plasma application is the simulation of dissociated gas flow thermochemical action on the thermal protection materials (TPMs) surfaces at the conditions of hypersonic re-entry flight [1-7]. IPM Plasma Laboratory has developed the program package for the complete numerical simulation of subsonic plasma flow (air, nitrogen, oxygen, carbon dioxide, argon) in the induction plasmatron and determination of surface catalycity of testing materials. This integral program package includes the codes Alpha, Beta and Gamma.

IPM approach is based on the fact that the whole flow in the induction plasmatron can be subdivided into three regions:

1) plasma flow within the discharge channel;

2) exhaust jet flow over a testing model in test chamber;

3) boundary layer in front of the model stagnation point.

Flow in each of the three regions has its own specific features:

- influence of radio frequency (RF) electromagnetic field is very important only in the first region;
- exhaust jet flow in front of the model is close to LTE when pressure is not too low;
- boundary layer in front of the model stagnation point is relatively thin and is essentially nonequilibrium (or frozen).

According to this subdivision, three different codes are used to calculate plasma flows within these three regions. The first two codes (Alpha and Beta) assume plasma flow to be under LTE conditions; the third code Gamma treats the boundary layer flow as chemically non-equilibrium with account for surface catalytic reactions.

Codes Alpha and Beta have been developed to calculate subsonic laminar equilibrium plasma flows in the discharge channel of induction plasmatron (Alpha) and in the exhaust jet flow over the testing model (Beta). Axial symmetry is assumed in both cases; cylindrical coordinate system is used to write the governing equations. Alpha is based on numerical solution of Navier-Stokes equations coupled with simplified Maxwell equations for RF electromagnetic field. Beta is based on numerical solution of Navier-Stokes equations. All the codes have been developed for geometry and experimental conditions of IPG-4 plasmatron.

The codes Alpha, Beta and Gamma provide the complete program package to determine:

- subsonic plasma flow parameters within the discharge channel including the exit section parameters (Alpha);
- jet flow parameters in plasmatron test chamber, in particular in the core of exhaust jet flow from the channel exit section to front face of the model, including dimensionless parameters at the external edge of boundary layer in front of the model to characterize flow vorticity and boundary layer thickness (Beta);
- heat flux to the model stagnation point or efficiency of surface recombination for testing material sample by the measured heat flux and surface temperature (Gamma). Also, Gamma code is used to rebuild flow enthalpy h_e through the measured heat flux q_{ws} to water-cooled calorimeter with silver surface (CO_2 flow) or copper surface (air flow). Here h_e is the flow enthalpy at the jet axis at the external boundary layer edge, q_{ws} is the heat flux measured to the standard high catalytic material; detailed description of the enthalpy rebuilding technique was presented in our previous SACOMAR report D5.4 [8].

Specific feature of IPM approach is the following. In result of Alpha and Beta codes solution, qualitative information on flow field pattern and temperature, enthalpy and velocity levels is obtained. But the main result provided by Alpha and Beta codes is the set of dimensionless parameters to characterize the boundary layer thickness, velocity, velocity gradient and flow vorticity at the external edge of boundary layer at the flow axis. These dimensionless parameters are necessary for the solution of boundary layer equations with account for finite layer thickness

with Gamma code. Actually, they are the interface between the first two codes and Gamma code. The key results - calculation of heat flux envelopes and determination of TPM surface recombination rates - are obtained with use of Gamma code coupled with experimental data on heat flux, surface temperature, and dynamic pressure. In the case when the direct measurement of flow enthalpy h_e is not available or is not accurate enough, the rebuilding of h_e is made also with use of Gamma code coupled with the necessary experimental data.

In the past years the code-to-code validations were made between Alpha code and CFD codes developed in the von Karman Institute for Fluid Dynamics (VKI) in Belgium [9,10], and in the Moscow Institute for Physics and Technology MIPT [11]. Comparison of Alpha & Beta codes calculations with CFD code developed in the Institute of Mechanics of the Lomonosov Moscow State University (IM MSU) was made in framework of INTAS-CNES project 03-53-5117 [12]. Note that IM MSU code was developed for both thermal and chemical nonequilibrium flow. The mentioned code-to-code comparisons were made for the cases of pure argon, air and CO_2 plasma flows in IPG-4 plasmatron, with use of simple geometry of discharge channel – cylindrical quartz tube without conic nozzle. The comparison of our calculation results obtained by Alpha and Beta codes with IPM experimental data for flow enthalpy and temperature for air and CO_2 working gases was made [13-15]. In total, comparisons of Alpha & Beta codes with CFD calculations of different scientific groups and with the experimental data showed the good accuracy of Alpha & Beta codes in the range of their applicability: pressure above 40-50 hPa, temperature below 8000 K.

Code-to-code validation between Gamma code and the code developed in the VKI showed a good (low enthalpy) and reasonable (high enthalpy) agreement between heat flux envelopes calculated for the dissociated CO_2 flow for the Mars entry conditions [16].

Below the detailed description is presented for Alpha, Beta and Gamma codes, including the problem formulation, boundary conditions, numerical solution techniques and some computation results for the four SACOMAR test regimes.

3 Numerical simulation of subsonic flow and electromagnetic field in IPG-4 discharge channel

Description of numerical simulation of subsonic flow and electromagnetic field in the discharge channel of IPG-4 plasmatron (realized in Alpha code) is subdivided into three parts: 1) gasdynamics - problem formulation for the Navier-Stokes equations; 2) electrodynamics - formulation of simplified Maxwell equations to calculate tangential component of the RF electric field amplitude; 3) numerical solution techniques used to solve Navier-Stokes and simplified Maxwell equations, and computation results for the four SACOMAR test regimes.

3.1 Gasdynamics

Alpha code was modified to calculate inductively coupled plasma flow within the segmented plasmatron discharge channel – the first computational region (see Fig.1). Note that the discharge channel itself (or torch) for IPG-4 plasmatron is 80-mm diameter quartz tube with inductor coil over it. The quartz tube passes into the water-cooling conical nozzle and short (80 mm) cylinder of 40 mm diameter (Fig. 1). This additional section was developed to provide the low enthalpy regimes. Gas is injected into the channel through the annular inlet slot adjacent to the wall; thickness of the slot is 2 mm. To provide the axial symmetry of the problem, the inductor coil is treated as five separate turns with the same current in each of them. Inductor turns are represented as thin equidistant rings perpendicular to the symmetry axis. Subsonic plasma flow in the discharge channel is assumed to be stationary, laminar and axisymmetric one with swirling in azimuthal direction. The flow is assumed to be under equilibrium conditions (both local thermal and chemical equilibrium is assumed); radiative processes are supposed to be negligible.

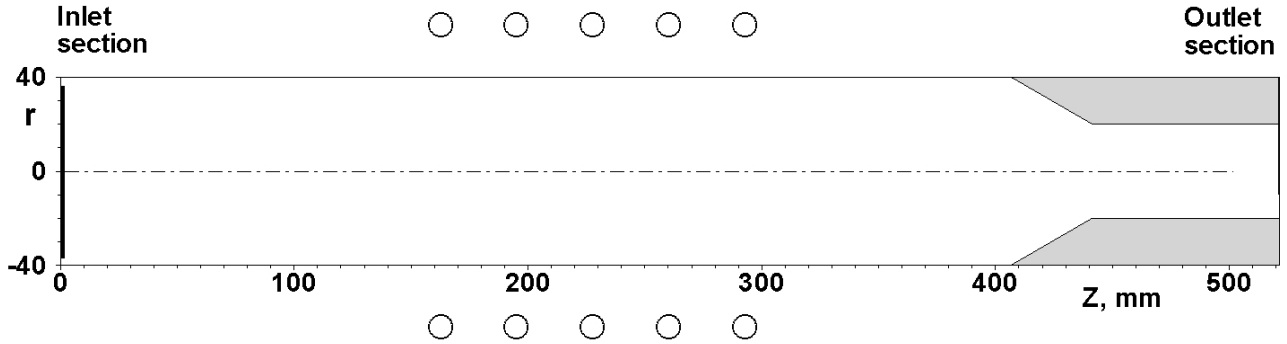

Figure 1: Schematic of IPG-4 discharge channel (first computational region).

The full Navier-Stokes equations written in the cylindrical coordinate system are used to simulate inductively coupled plasma (ICP) flow in the discharge channel. We assume that Navier-Stokes equations are time-averaged with respect to RF oscillations of the inductor current.

The resulting governing equations are two-dimensional Navier-Stokes equations with account for three velocity components - axial, radial and tangential component due to the flow spinning, together with energy equation written for the total gas enthalpy.

Continuity equation:

$$\frac{\partial}{\partial z}(\rho u)+\frac{1}{r}\frac{\partial}{\partial r}(r\rho v)=0 \tag{1}$$

Axial momentum equation:

$$\begin{aligned}&\frac{\partial}{\partial z}(\rho uu)+\frac{1}{r}\frac{\partial}{\partial r}(r\rho uv)=-\frac{\partial}{\partial z}\left(P+\frac{2}{3}\mu\left[\frac{\partial u}{\partial z}+\frac{1}{r}\frac{\partial rv}{\partial r}\right]\right)+\\&+2\frac{\partial}{\partial z}\left(\mu\frac{\partial u}{\partial z}\right)+\frac{1}{r}\frac{\partial}{\partial r}\left(r\mu\left(\frac{\partial u}{\partial r}+\frac{\partial v}{\partial z}\right)\right)+F_z\end{aligned} \tag{2}$$

Radial momentum equation:

$$\begin{aligned}&\frac{\partial}{\partial z}(\rho uv)+\frac{1}{r}\frac{\partial}{\partial r}(r\rho vv)=-\frac{\partial}{\partial r}\left(P+\frac{2}{3}\mu\left[\frac{\partial u}{\partial z}+\frac{1}{r}\frac{\partial rv}{\partial r}\right]\right)+\\&+\frac{\partial}{\partial z}\left(\mu\left(\frac{\partial v}{\partial z}+\frac{\partial u}{\partial r}\right)\right)+\frac{2}{r}\frac{\partial}{\partial r}\left(r\mu\frac{\partial v}{\partial r}\right)-\frac{2\mu v}{r^2}+\frac{\rho w^2}{r}+F_r\end{aligned} \tag{3}$$

Tangential momentum equation:

$$\frac{\partial}{\partial z}(\rho uw)+\frac{1}{r}\frac{\partial}{\partial r}(r\rho vw)=\frac{\partial}{\partial z}\left(\mu\frac{\partial w}{\partial z}\right)+\frac{1}{r}\frac{\partial}{\partial r}\left(r\mu\frac{\partial w}{\partial r}\right)-\frac{\rho vw}{r}-\frac{w}{r^2}\frac{\partial}{\partial r}(r\mu) \tag{4}$$

Energy equation:

$$\frac{\partial}{\partial z}(\rho uh)+\frac{1}{r}\frac{\partial}{\partial r}(r\rho vh)=\frac{\partial}{\partial z}\left(\frac{\mu}{\mathrm{Pr}_{eff}}\frac{\partial h}{\partial z}\right)+\frac{1}{r}\frac{\partial}{\partial r}\left(\frac{r\mu}{\mathrm{Pr}_{eff}}\frac{\partial h}{\partial r}\right)+Q_J \tag{5}$$

Here: z and r are the axial and radial coordinates; u, v, w – the axial, radial and tangential velocity components; P, ρ, h, μ - the pressure, density, enthalpy and viscosity of equilibrium gas mixture, Pr_{eff} is the effective Prandtl number.

These equations include time-averaged source terms corresponding to RF electromagnetic field influence: F_z, F_r are axial and radial components of the Lorentz force; Q_J is Joule heat production.

These source terms are expressed via E_θ - tangential component of the complex amplitude of vortical electric field:

$$F_z = -\frac{\sigma}{2\omega}\mathrm{Re}\left\{E_\theta\left(i\frac{\partial E_\theta}{\partial z}\right)^*\right\},\quad F_r = -\frac{\sigma}{2\omega}\frac{1}{r}\mathrm{Re}\left\{E_\theta\left(i\frac{\partial rE_\theta}{\partial r}\right)^*\right\},\quad Q_J = \frac{\sigma}{2}E_\theta E_\theta^* \tag{6}$$

here Re means the real part of a complex value, asterisk is the conjugation sign for a complex value, ω - the circular frequency of monochromatic electric field, σ - the plasma electrical conductivity.

Boundary conditions for the gasdynamic equations:

- All the necessary flow parameters including velocity tangential component (to provide the flow spinning) are specified at the discharge channel entry section. These specified parameters are the following:

  $\rho_0 u_0 = G / A_{SL}$, here G - specified gas flow rate,

  A_{SL} - area of the annular inlet slot with the thickness 2 mm;

  $v_0=0$;

  T_0 – the temperature of the injecting gas at the annular inlet slot (T_0 = 300 K);

  P_0 – the static pressure specified at inflow section at the symmetry axis;

  θ_0 = 45° – the swirl angle of the injecting gas at the inlet slot, $\frac{w_0}{u_0} = tg(\theta_0)$;

  (here subscript "0" refers to gas parameters at the channel inlet section).

- Zero values for the velocity components are specified at all rigid surfaces - quartz tube wall, wall of the second section of the channel with the conic nozzle; face of the gas injector interface at the channel inlet section:

  $u_w = v_w = w_w = 0$; here subscript "w" refers to any rigid wall;

- Symmetry conditions are applied at the channel axis:

$$v(z,0) = w(z,0) = 0;\quad \frac{\partial u}{\partial r}(z,0) = \frac{\partial h}{\partial r}(z,0) = 0 \tag{7}$$

- Soft conditions are applied at the channel exit section (outlet) $z = Z_C$, i.e. the unknown functions are extrapolating outside the calculation region:

$$\frac{\partial u}{\partial z}(z_c,0) = \frac{\partial v}{\partial z}(z_c,0) = \frac{\partial w}{\partial z}(z_c,0) = \frac{\partial h}{\partial z}(z_c,0) = 0 \tag{8}$$

- Definite values of temperature are specified at all rigid surfaces:
  - ♦ $T=T_{WIF}$ - the specified value of wall temperature at the inlet face wall,
  - ♦ $T=T_{WQ}$, - the specified value of the quartz wall temperature;
  - ♦ $T=T_{WC}$, - the specified value of the wall temperature of the second section of the channel with the conical nozzle.

In calculations for the specified SACOMAR test regimes we used common assumption that $T_{WIF}=T_{WQ}=T_{WC}=T_W=300$ K. Actual values of T_{WIF} and T_{WQ} are higher, but our previous numerical investigations showed that the influence of higher values of T_{WIF} and T_{WQ} is essential only in a small regions adjacent to the corresponding surfaces and does not effect the flow parameters at the discharge channel exit section.

3.2 Electrodynamics

Suppose that RF oscillating inductor current is composed of a single Fourier mode and it produces a monochromatic electric field with complex amplitude:

$$\vec{E}(t,z,r) = \vec{E}(z,r)\cdot\exp(-i\omega t), \quad \vec{H}(t,z,r) = \vec{H}(z,r)\cdot\exp(-i\omega t) \tag{9}$$

here $\omega = 2\pi f$ - the circular frequency, f – the frequency of the inductor current, t – the time. Here we use complex values of $\vec{E}$ and $\vec{H}$ amplitudes.

The following common assumptions are used:

- plasma is quasi-neutral;
- plasma magnetic permeability $\mu = 1$;
- plasma dielectric constant does not depend on the electromagnetic field and so does not depend on z and r;
- the displacement current is negligible;
- inductor coil is represented by a series of parallel current-carrying rings to provide the axial symmetry for the problem; the rings are assumed to be infinitely thin; a single coil current with the same amplitude and phase angle is assumed to oscillate through each of coil rings.

Following Boulos [17], we use also the assumption: $\partial E_\theta / \partial z << \partial E_\theta / \partial r$, that leads (with account for symmetry conditions) to quasi-one-dimensional approximation of Maxwell equations [18-20]:

$$\frac{d}{dr}\left(\frac{1}{r}\frac{d}{dr}\left(rE_\theta\right)\right) = -i\omega\mu_0\sigma E_\theta \tag{10}$$

$$E_z = 0, \quad E_r = 0, \quad i\omega\mu_0 H_z = \frac{1}{r}\frac{d}{dr}\left(rE_\theta\right)$$

Here E_z, E_r, E_θ are axial, radial and tangential components of the electric field amplitude; H_z is axial component of the magnetic field amplitude, μ_0 is the magnetic constant (vacuum permeability). Equation (10) together with appropriate boundary conditions (11-12) (see below) is used in our method to determine electromagnetic field amplitudes E_θ and H_z.

The obtained quasi-1D approximation is essential simplification for the problem, it leads to boundary value problem for the ordinary differential equation (10) to determine complex amplitude of the electric field $E_\theta(z, r)$; z coordinate is only a parameter in this equation, E_θ depends on z owing to the boundary conditions. In this approximation the axial component of the Lorentz force F_z equals to zero.

Note that for the equilibrium plasma it's electric conductivity $\sigma = \sigma(P,T)$, so $\sigma(P,T)$ serves here as interface between the gasdynamic and electrodynamic subsystems of the governing equations.

Boundary conditions for the equation (10) are the symmetry condition at the axis

$$E_\theta(z,0) = 0 \tag{11}$$

and the following condition at the discharge channel wall:

$$r = R_c: \quad \frac{1}{r}\frac{d}{dr}\left(rE_\theta\right) = i\omega\mu_0 H_{zw0}(z) \tag{12}$$

here R_C is the channel radius (R_C =40 mm within the quartz tube, than it is decreases to 20 mm after the conic nozzle), H_{ZW0} is the amplitude of the magnetic field axial component at the channel wall produced only by the inductor current outside the plasma flow.

It is important to note that the comparison of accurate electrodynamic model results [21] (the full two-dimensional Maxwell equations were solved on a far field domain) with our results obtained

with use of the quasi-1D model (10-12) demonstrated a good accuracy of this simplified model in wide range of operating frequency and pressure. Differences of a few percent between the results were observed in the inlet region and at the mid-coil position; practically no differences were observed at the torch outlet. The comparison was made for the IPG-4 plasma torch geometry and reported in details in [9].

3.3 Numerical solution technique and computation results for the test regimes

Alpha solves finite-difference approximations to the governing equations.

Navier-Stokes equations solution technique is based on the control volumes method and SIMPLE algorithm of Patankar and Spalding with use of the staggered grid [22-23]. Convective terms are approximated by the finite differences with the first order accuracy. Some necessary modifications of the Patankar & Spalding method were made to provide the convergence of iterations for a complicated ICP flow with large vortices. In particular, the unknown functions are determined with use of additional under-relaxation procedure to increase stability of the solution technique [20]. The strong convergence of iterations should be provided: normally we require basic flow parameters to be converged up to 1e-9.

Non-uniform rectangular computation grid can be used both in axial and radial directions. The grid is condensed in radial direction near the torch wall; the grid is condensed in axial direction near the torch inlet section and within the inductor region. Sometimes, the uniform grid in both directions is used in case of large numbers of grid points in axial and radial directions.

Thomas algorithm ("sweep" algorithm) for 3-diagonal matrix equations with use of complex variables is applied to solve the boundary value problem for the equation (10) to obtain the complex value of the electric field amplitude E_θ.

Value of the inductor current is determined in process of iterations by the prescribed value of power input in plasma N_{pl}. As to a value of N_{pl} itself, it should be specified by both the measured value of anode power N_{ap} and the plasmatron efficiency η_{eff} obtained from special experimental measurements: $N_{pl} = \eta_{eff} * N_{ap}$.

The necessary thermodynamic and transport properties are determined simultaneously in the process of numerical solution for each grid point by the interpolation procedure across the previously calculated tables. These tables for equilibrium 97%CO_2+3%N_2 (or pure CO_2) gas mixture properties have been calculated in advance as functions of pressure and temperature (see below, chapter 5). This approach provides rather accurate values for plasma transport coefficients with minimum increase in CPU time.

Computation results for 97%CO_2+3%N_2 and pure CO_2 plasma flows in IPG-4 discharge channel for the four specified SACOMAR test regimes (Table 1) are presented in the Figs. 2-7.

Table 1: Test regimes realized in IPG-4 facility (IPM).

P, hPa	N_{ap}, kW	N_{pl}, kW	Zm, mm	h_e, MJ/kg
80	40.4	20.28	40	14.0
80	34.0	16.45	40	8.8
40	35.0	17.05	72	14.4
40	35.0	17.05	122	9.5

The geometry of the first section of the discharge channel is the following: 80 mm diameter cylinder (quartz tube) with 406 mm length; Z_{ind} = 205 mm is the distance from the entry section to the first turn of inductor; L_{ind} = 130 mm is the length of inductor coil; D_{ind} = 120 mm is the diameter of inductor coil. The second section of the discharge channel is the sonic cylindrical nozzle with 30° half angle and short cylinder (80 mm length) after it. The total length of the two-section discharge channel is 521 mm.

The IPG-4 inductor current frequency f = 1.76 MHz.

The uniform rectangular computation grid of 162*82 points was used for the four SACOMAR test regimes (i.e. 163 points are used in radial direction for the whole channel region due to the axial symmetry). The CPU time for Alpha code run is about 40-50 minutes for AMD Athlon X2 Dual Core PC, 3.8 GHz, about 30000 iterations is done, the basic flow parameters are converged to 1e-9.

Isolines of the dimensionless stream function and isotherms in IPG-4 discharge channel for the three test regimes with 97%CO_2+3%N_2 working gas are shown in Figs. 2-4. Isolines of the dimensionless stream function are shown in top parts of the figures (a) to visualize the complicated structure of ICP vortical flow: secondary vortex is formed near the inlet section, and large primary vortex (with negative values of stream function f) is formed between the secondary vortex and the inductor region. Values of the dimensionless stream function f are shown on isolines; note that the dimensionless stream function f(z, r) reaches its maximum value f=1 at the torch wall.

The plasma temperature fields (isotherms) are shown in the bottom parts of the figures (b). Temperature values for isotherms are given in K. The maximum of temperature is located within the inductor region close to the symmetry axis, it is shown by red dots or small spots.

The corresponding streamlines and isotherms calculated for pure CO_2 flow are not shown because they are practically identical to the results for 97%CO_2+3%N_2 flow.

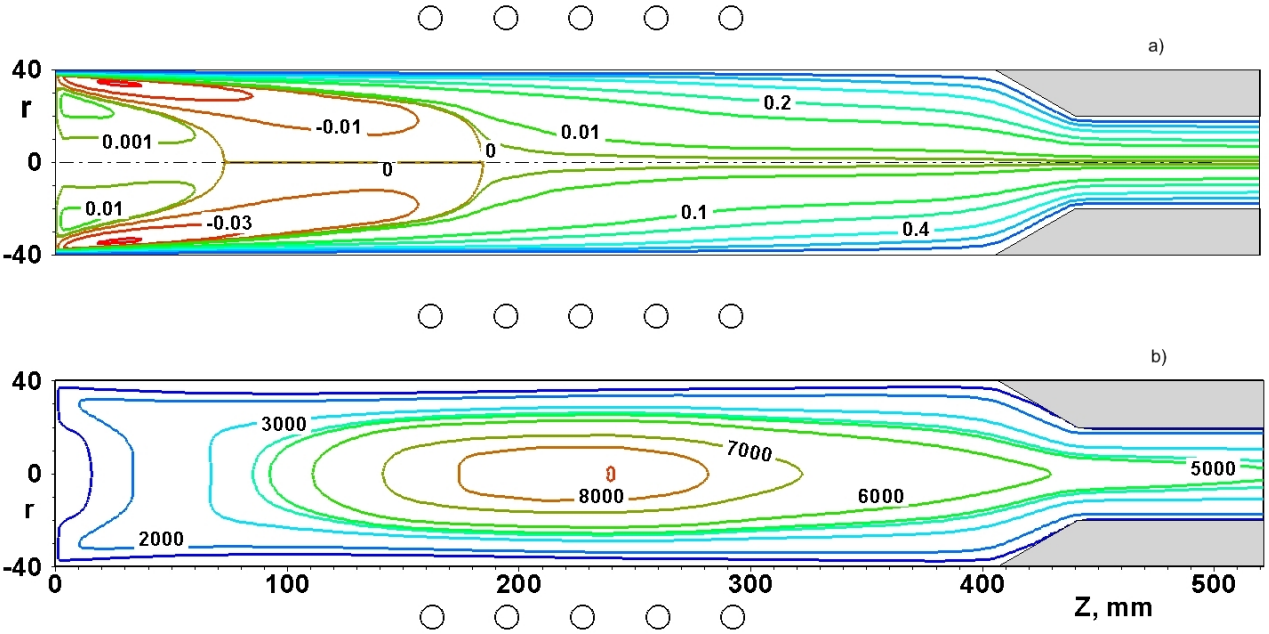

Figure 2: Isolines of stream function (a) and isotherms (b) in IPG-4 discharge channel, 97%CO_2+3%N_2 flow, P=80 hPa, N_{pl}=20.28 kW.

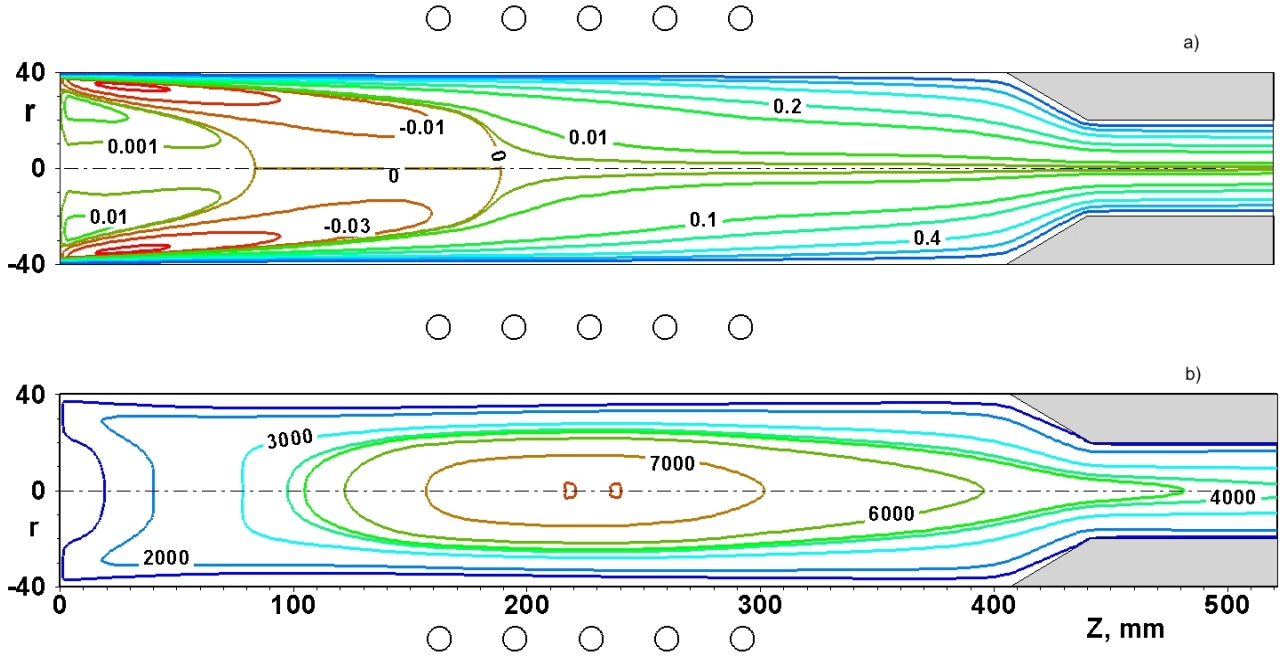

Figure 3: Isolines of stream function (a) and isotherms (b) in IPG-4 discharge channel, 97%CO_2+3%N_2 flow, P=80 hPa, N_{pl}=16.45 kW.

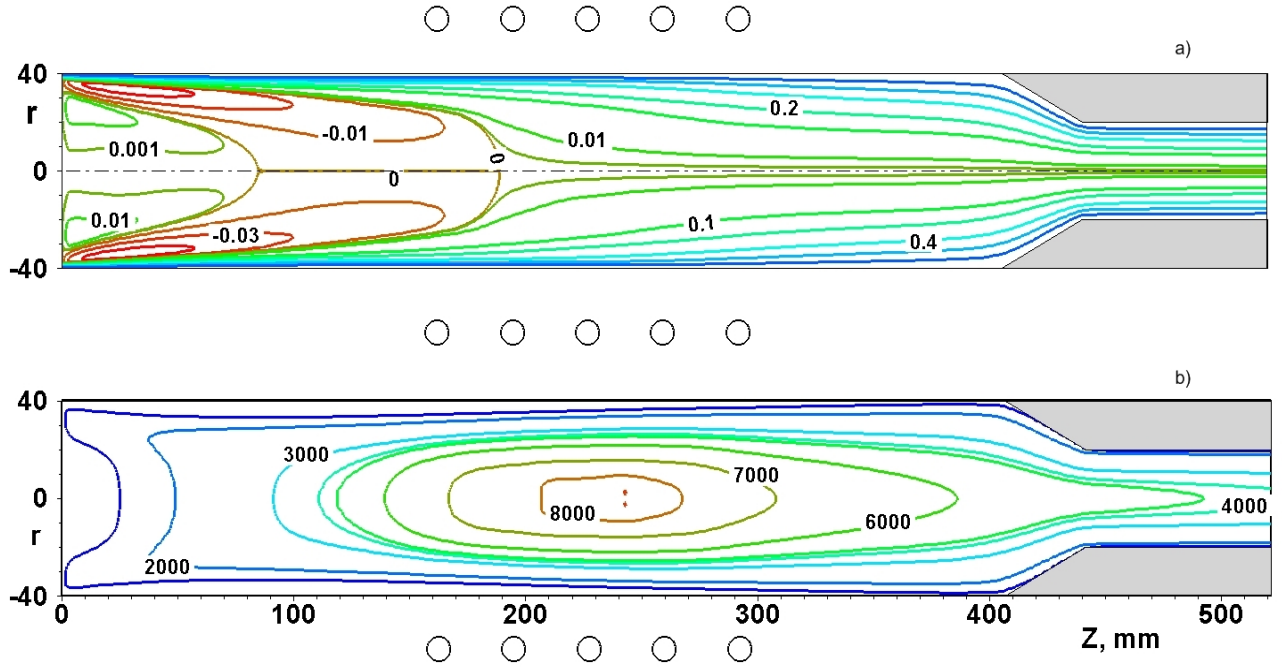

Figure 4: Isolines of stream function (a) and isotherms (b) in IPG-4 discharge channel, 97%CO_2+3%N_2 flow, P=40 hPa, N_{pl}=17.05 kW.

Radial profiles of calculated plasma parameters in the discharge channel exit section are shown in Figs. 5-7: axial velocity $u(Z_C, r)$ - Fig. 5; enthalpy $h(Z_C, r)$ - Fig. 6, and temperature $T(Z_C, r)$ - Fig. 7. Here Z_c=521 mm is the channel length. The colored curves are the results obtained for 97%CO_2+3%N_2 flow for SACOMAR test regimes, black dash curves are the results for the same regimes for pure CO_2 flow.

Blue curves with circles are the results for IPG-4 regime P=40 hPa, N_{pl}=17.05 kW;

red curves with triangles: P=80 hPa, N_{pl}=20.28 kW;

magenta curves with squares: P=80 hPa, N_{pl}=16.45 kW.

It is clear that the discrepancy between the results obtained for 97%CO_2+3%N_2 and pure CO_2 flows is negligible: the maximum difference is about 1% and 2% for velocity and temperature profiles, but the enthalpy profiles are practically identical.

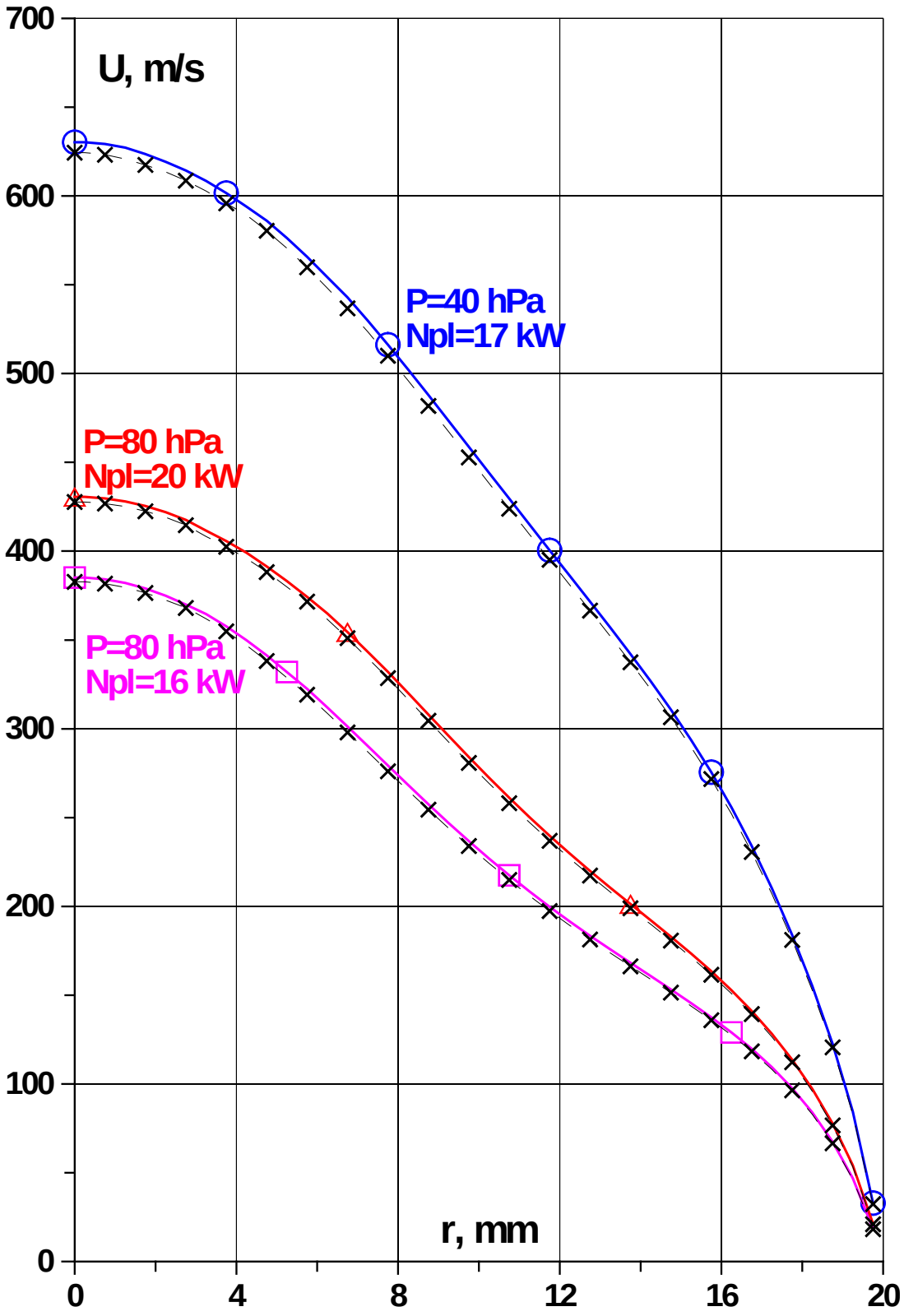

Figure 5: Radial velocity profiles at the discharge channel exit section.

Colored curves are velocity at the jet axis for 97%CO_2+3%N_2 flow, black dash curves are similar results for pure CO_2 flow. Blue curves with circles: P=40 hPa, N_{pl}=17.05 kW; red curves with triangles: P=80 hPa, N_{pl}=20.28 kW; magenta curves with squares: P=80 hPa, N_{pl}=16.45 kW.

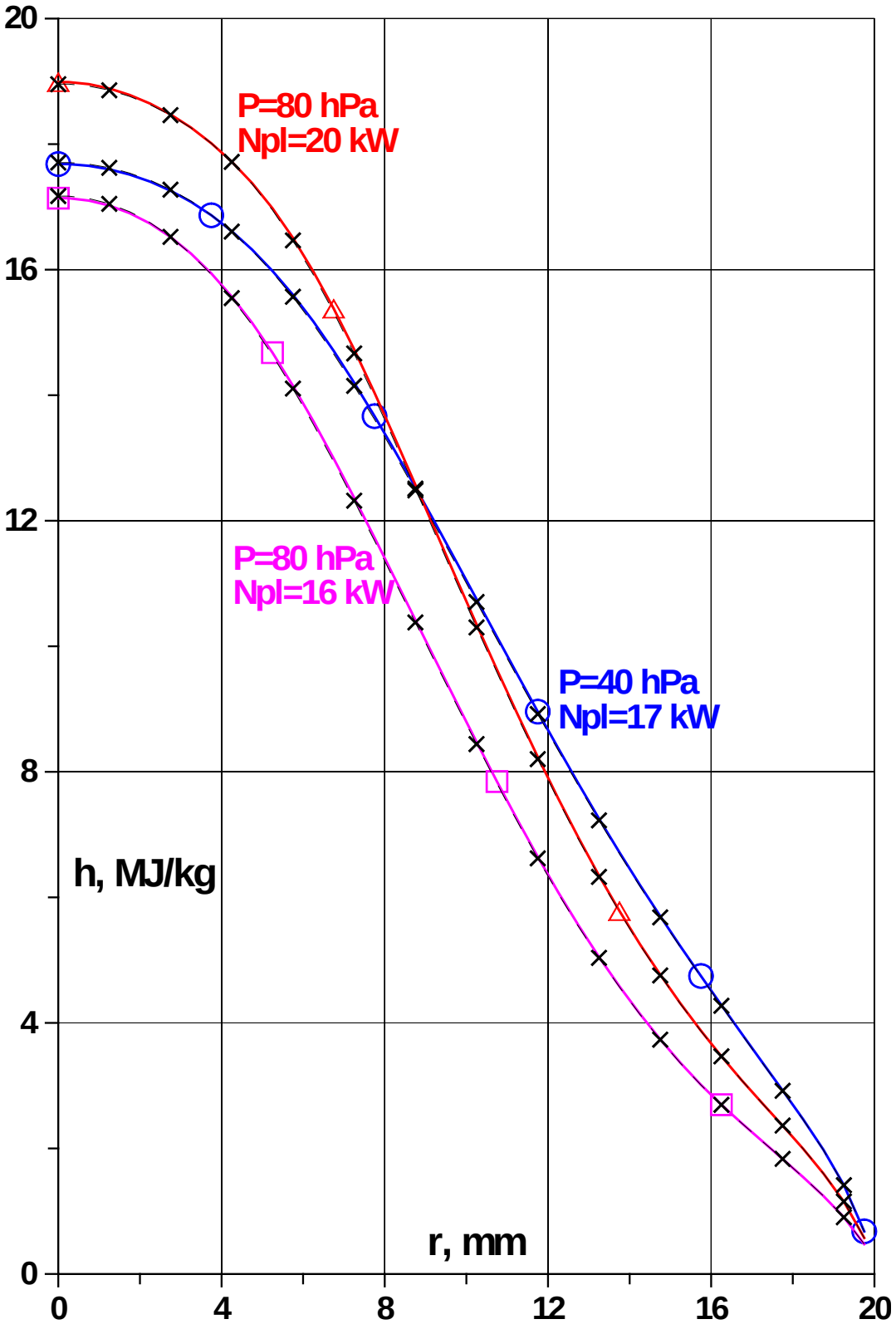

Figure 6: Radial enthalpy profiles at the discharge channel exit section.

Colored curves are enthalpy at the jet axis for 97%CO_2+3%N_2 flow, black dash curves are similar results for pure CO_2 flow. Blue curves with circles: P=40 hPa, N_{pl}=17.05 kW; red curves with triangles: P=80 hPa, N_{pl}=20.28 kW; magenta curves with squares: P=80 hPa, N_{pl}=16.45 kW.

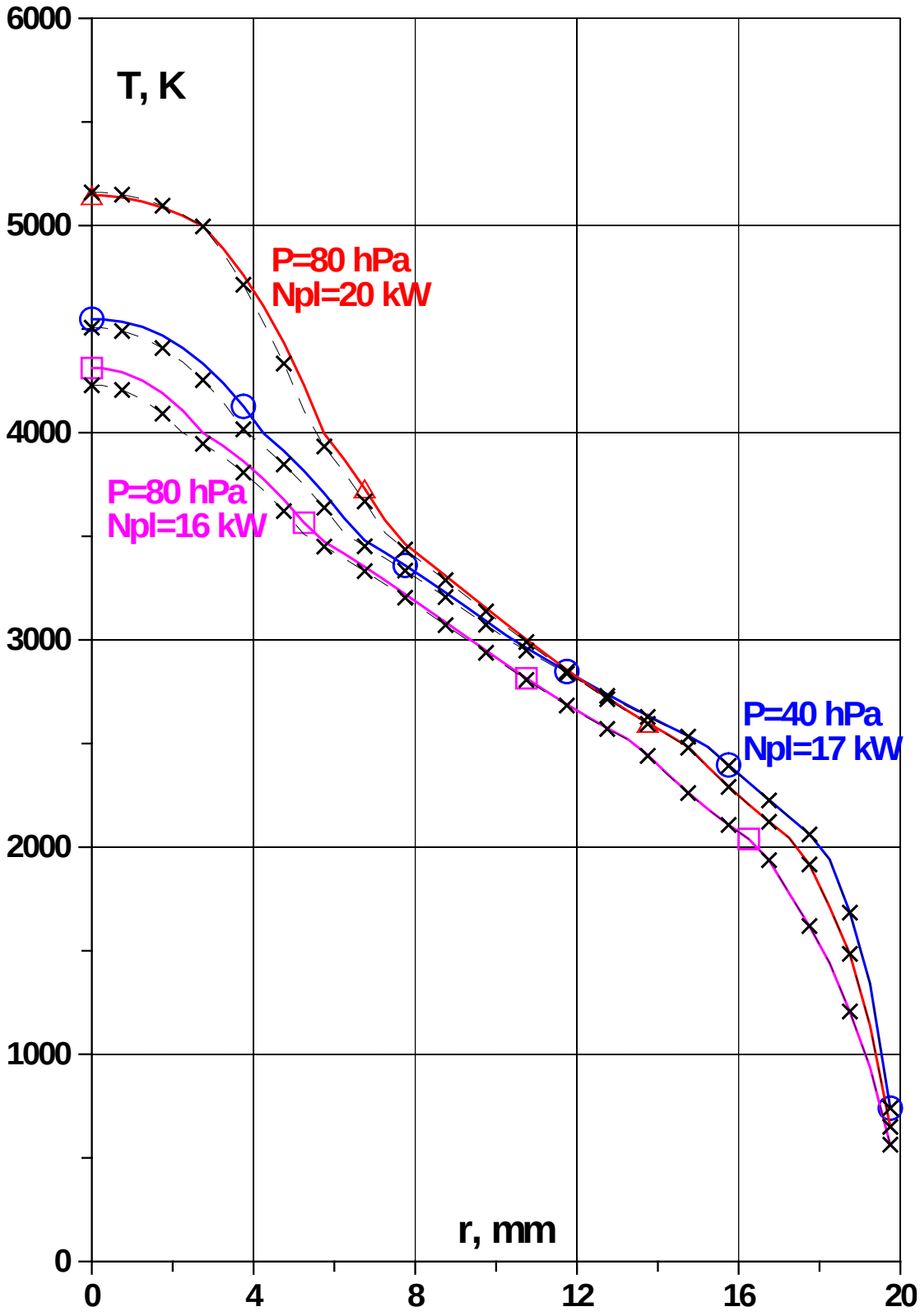

Figure 7: Radial temperature profiles at the discharge channel exit section.

Colored curves are temperature at the jet axis for 97%CO_2+3%N_2 flow, black dash curves are similar results for pure CO_2 flow. Blue curves with circles: P=40 hPa, N_{pl}=17.05 kW; red curves with triangles: P=80 hPa, N_{pl}=20.28 kW; magenta curves with squares: P=80 hPa, N_{pl}=16.45 kW.

4 Numerical simulation of subsonic jet flow over testing model

4.1 Gasdynamics

Beta code is developed to calculate the dissociated gas flow in the second computational region, i.e. to calculate the subsonic exhaust jet flow over testing model in IPG-4 test chamber after the discharge channel exit section (Fig. 8).

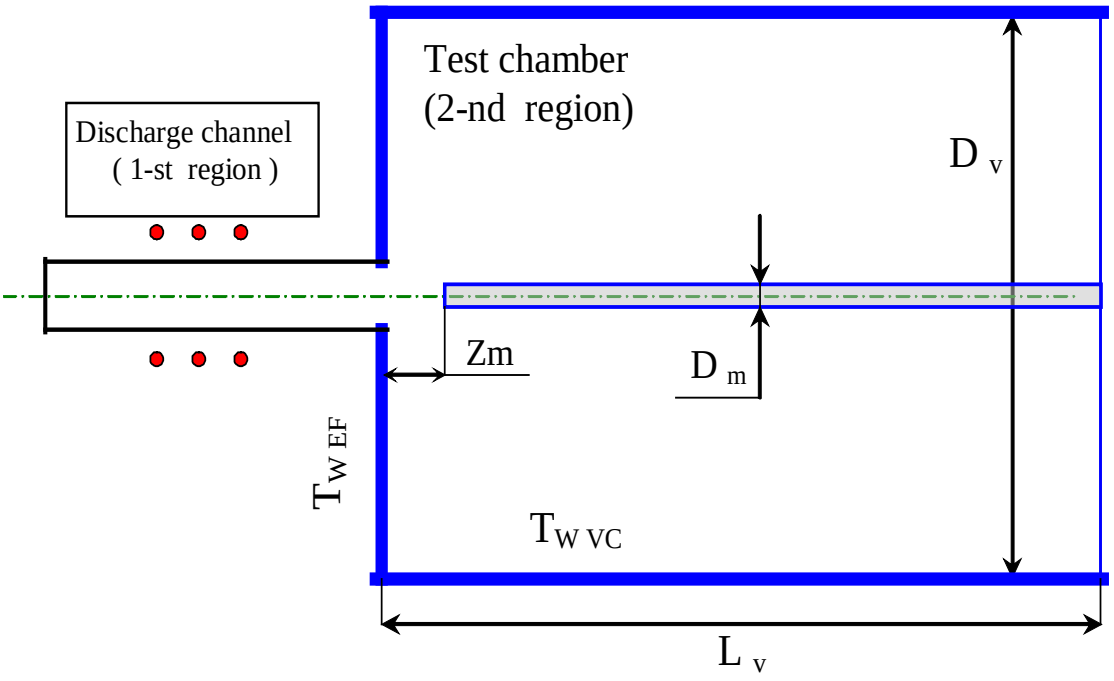

Figure 8: Schematic of IPG-4 test chamber and model (the second computational region).

Subsonic jet flow over the testing model in test chamber is assumed to be stationary, laminar and axisymmetric one with no account for swirl in azimuthal direction; we assume that influence of azimuthal swirling is negligible outside the discharge channel due to the large diameter of the chamber. The exhaust jet flow over the model is assumed to be under thermal and chemical equilibrium conditions, and radiative processes are supposed to be negligible.

We assume that the model flowed over in the test chamber is the long cylinder with the blunted front face (e.g. the standard 50-mm diameter ESA model with rounded edges) or with the flat front face.

Influence of RF electromagnetic field is assumed to be negligible outside the discharge channel, so the equations presented below do not have source terms corresponding to Lorentz force and Joule heat production.

The full Navier-Stokes equations written in the cylindrical coordinate system are used to simulate the exhaust jet flow. These governing equations are two-dimensional ones with account for two velocity components – axial and radial, together with energy equation written for the total gas enthalpy. These equations can be easily obtained from the equations (1) - (5) presented in the previous chapter 3 under the condition that Lorentz force and Joule heat production are negligible in the second region outside the discharge channel.

Boundary conditions for the Navier-Stokes equations in the second region are the following:

- All the necessary flow parameters should be specified at the discharge channel outlet section as the inflow parameters for the exhaust jet flow in the test chamber.

These parameters - $u_c(r)$; $P_c(r)$, $h_c(r)$; ρ_c (r) – should be calculated in advance by Alpha code; here subscript "c" refers to gas parameters at the channel exit section. Radial velocity component calculated by Alpha code is assumed to be equal to zero at the channel exit section.

Due to the difference between the first computation grid used within the discharge channel (Alpha code) and the grid used within the second region (Beta code), the inflow parameters for Beta code are determined by interpolation procedure across the corresponding flow parameters calculated previously by Alpha code at the channel exit section - Alpha results are remapped from the first grid onto the second grid.

- Zero values for the velocity components are specified at all rigid surfaces:

$u_w = v_w = 0$; here subscript "w" refers to any rigid wall;

- Definite values of temperature are specified at all rigid surfaces (test chamber side wall; interface between the discharge channel outlet section and the test chamber; model surface):

$T_W = T_{W\,VC}$ - temperature of the test chamber side wall;

$T_W = T_{W\,EF}$ - temperature of the entry face wall (the wall between discharge channel exit section and test chamber side wall;

$T_W = T_{W\,MOD}$ - temperature of the model surface.

- Symmetry conditions are applied at the channel axis:

$$v(z,0) = 0, \quad \frac{\partial u}{\partial r}(z,0) = \frac{\partial h}{\partial r}(z,0) = 0;$$

- "Soft" outlet conditions are applied at the exit section of the second computation region $z = L_V$, i.e. the unknown functions are extrapolating outside the calculation region:

$$\frac{\partial u}{\partial z}(L_v, 0) = \frac{\partial v}{\partial z}(L_v, 0) = \frac{\partial h}{\partial z}(L_v, 0) = 0$$

Note that influence of the temperature boundary conditions (values of $T_{W\,VC}$, $T_{W\,EF}$, $T_{W\,MOD}$) on the flow parameters in the core of the jet in front of the model is quite small. For example, change of the cool wall boundary condition $T_{W\,EF}$ = 300 K by the adiabatic entry face wall condition

$$\left.\frac{\partial T}{\partial z}\right|_{z=0\,(entry\ \ face\ wall)} = 0$$

will lead to essential changes in flow field in the whole test chamber, except the region in question - the core of the jet in front of the model. Also, influence of other temperature conditions ($T_{W\,VC}$, $T_{W\,MOD}$) on the plasma jet in front of the model is quite small. But, plasma parameters in this small region in the core of the jet in front of the model are the most important result of Beta code. Therefore, the standard temperature boundary conditions

$T_{W\,VC} = T_{W\,EF} = T_{W\,MOD} = 300$ K

can be used to run Beta code with no loss of accuracy for the main results - plasma parameters in the core of the jet in front of testing model, including the dimensionless parameters at the boundary layer external edge to be used further as the input data for Gamma code.

Also, influence of the test chamber diameter and it's length on the main Beta results (plasma parameters in the core of the jet in front of testing model) is quite small, provided that $D_V >> D_M$ and $L_V > D_V$. Here L_v and D_v – length and diameter of the second computation region (they can be treated as "effective" values of the test chamber length and diameter); Zm – distance from the model to the torch exit; R_M and D_M – radius and diameter of the testing model (Fig. 8).

Note that if the testing model is placed too close to the discharge channel exit section ($Zm < R_M$), the results of Alpha & Beta calculations could be not accurate. Separate calculation of the flows in the first and second regions is possible only if Zm is greater than R_M and R_C. Otherwise, both first and second regions should be calculated by a special single code as the single computation region (or as the two coupled regions). On the other hand, Zm should not be too large, because the turbulence effects should be accounted at large distances along the jet.

4.2 Numerical solution technique and computation results

The same solution technique as for Alpha code is used here to solve Navier-Stokes equations. It is based on the control volumes method and SIMPLE algorithm of Patankar and Spalding with use of the staggered grid [22-23]. Unknown functions are determined with use of under-relaxation procedure to increase a stability of the solution technique.

The necessary thermodynamic and transport properties are determined simultaneously in the process of numerical simulation for each grid point by the interpolation procedure across the previously calculated tables, just the same as for the Alpha code; details are given below in chapter 5.

Nonuniform rectangular grid spacing is used both in axial and radial directions. Computation grid is condensed in axial direction near the front surface of the model to provide sufficient number of grid points in the distance between the torch exit and the model, and especially within the boundary layer in front of the model.

The grid is condensed in radial direction near the symmetry axis (i.e. in the core of the jet) and also near the side wall of the model.

To provide a possibility to change easily the position of the model Zm, the chamber diameter D_V and length L_V, the special algorithm was developed in Beta code to fit the computation grid to the changed geometry, i.e. to construct a nonuniform mesh adaptive to the model position and chamber dimensions.

Note that the Patankar & Spalding method with use of "soft" boundary conditions at the outlet boundary could be applied efficiently only if the length of the computation region is greater than its diameter. So, the following condition must be fulfilled to provide accuracy of the method: $L_V > D_V$. Actually, the condition $L_V \geq 1.5 * D_V$ is used in Beta code to increase the efficient chamber length, if necessary.

IPG-4 test chamber geometry is specified as follows: Z_V = 1200 mm; D_V = 800 mm.
Standard temperature boundary conditions were used: $T_{W\,VC} = T_{W\,EF} = T_{W\,MOD}$ = 300 K.
Euromodel geometry is as follows: diameter D_m = 50 mm; radius for edge rounding R_{rnd} = 11 mm.
The model position Zm is 40mm for P=80 hPa test regimes, Zm varies from 72 to 122 mm for P=40 hPa test regimes.

Nonuniform computation grid of 103 points was used in radial direction, and from 103 to 113 points was used in axial direction for different Zm values.

Computational grid in the part of computation region - in the core of the jet in front of the model is shown in Fig. 9 for the case of Zm=40 mm.

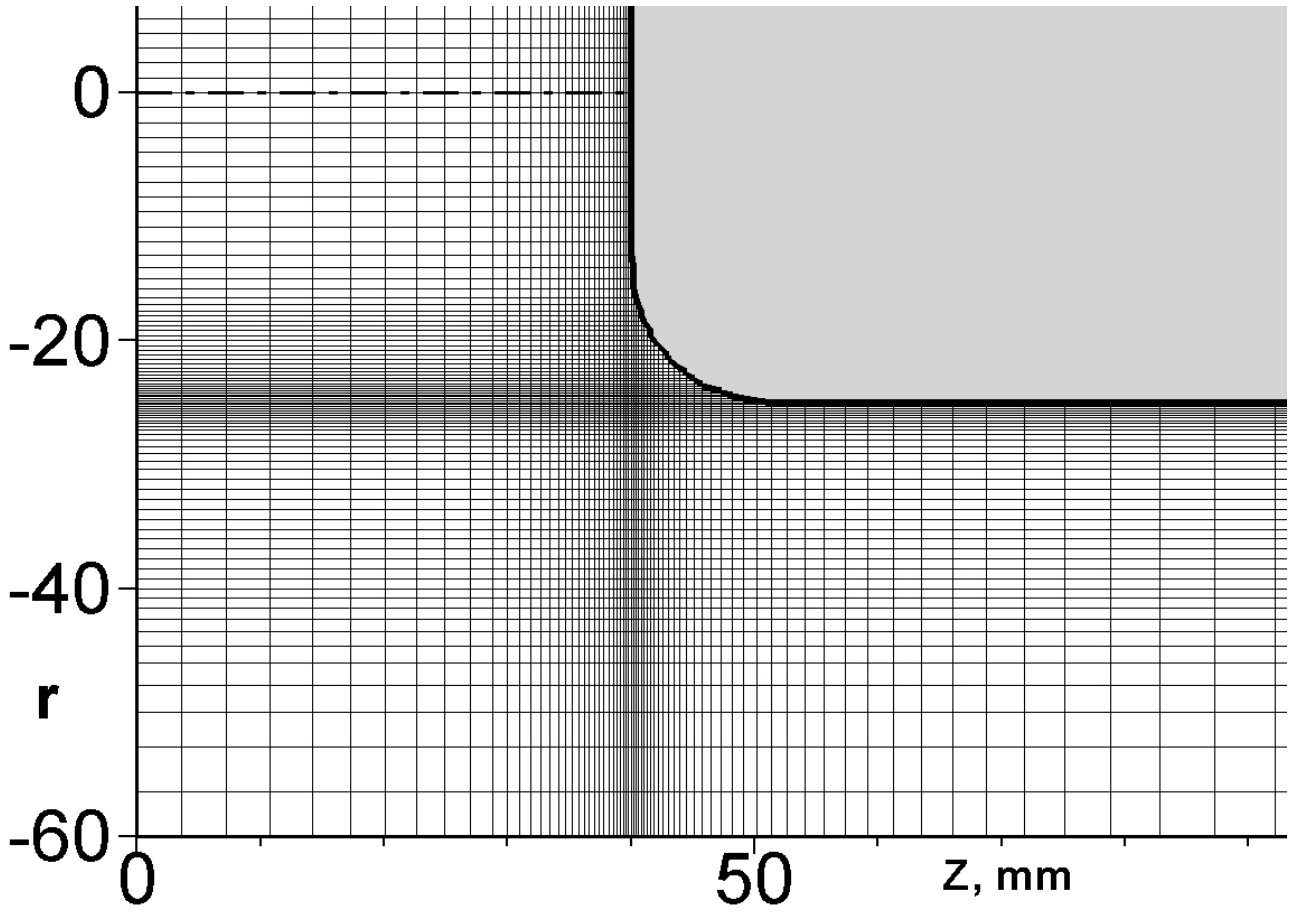

Figure 9: Computational grid in the core of the jet in front of euromodel for Zm=40 mm.

CPU time for Beta run is about 30 minutes, about 30000 iterations are done, the basic flow parameters are converged to 1e-9.

Computation results for subsonic exhaust jet flow over euromodel in IPG-4 test chamber are presented in Figs. 10-13 (streamlines and isotherms) and Figs. 14-18 (axial distribution of flow parameters from the channel exit section to the model). The Beta calculations were made for the same SACOMAR test regimes shown above in Table 1; the previously obtained results at the channel exit section (Alpha) are used as inflow data for Beta calculations.

Normalized stream function contours (a) and isotherms (b) for the jet flow over euromodel for the four SACOMAR test regimes with 97%CO_2+3%N_2 flow are shown in Figs. 10-13. The results are presented not for the whole computation region but only for the core of the jet in front of the model. The position of the inlet, i.e. the discharge channel exit section diameter (40 mm) is shown by red lines at the left of the computational region.

The streamlines and isotherms calculated for the pure CO_2 flow are not shown because they are practically identical to that for 97%CO_2+3%N_2 flow.

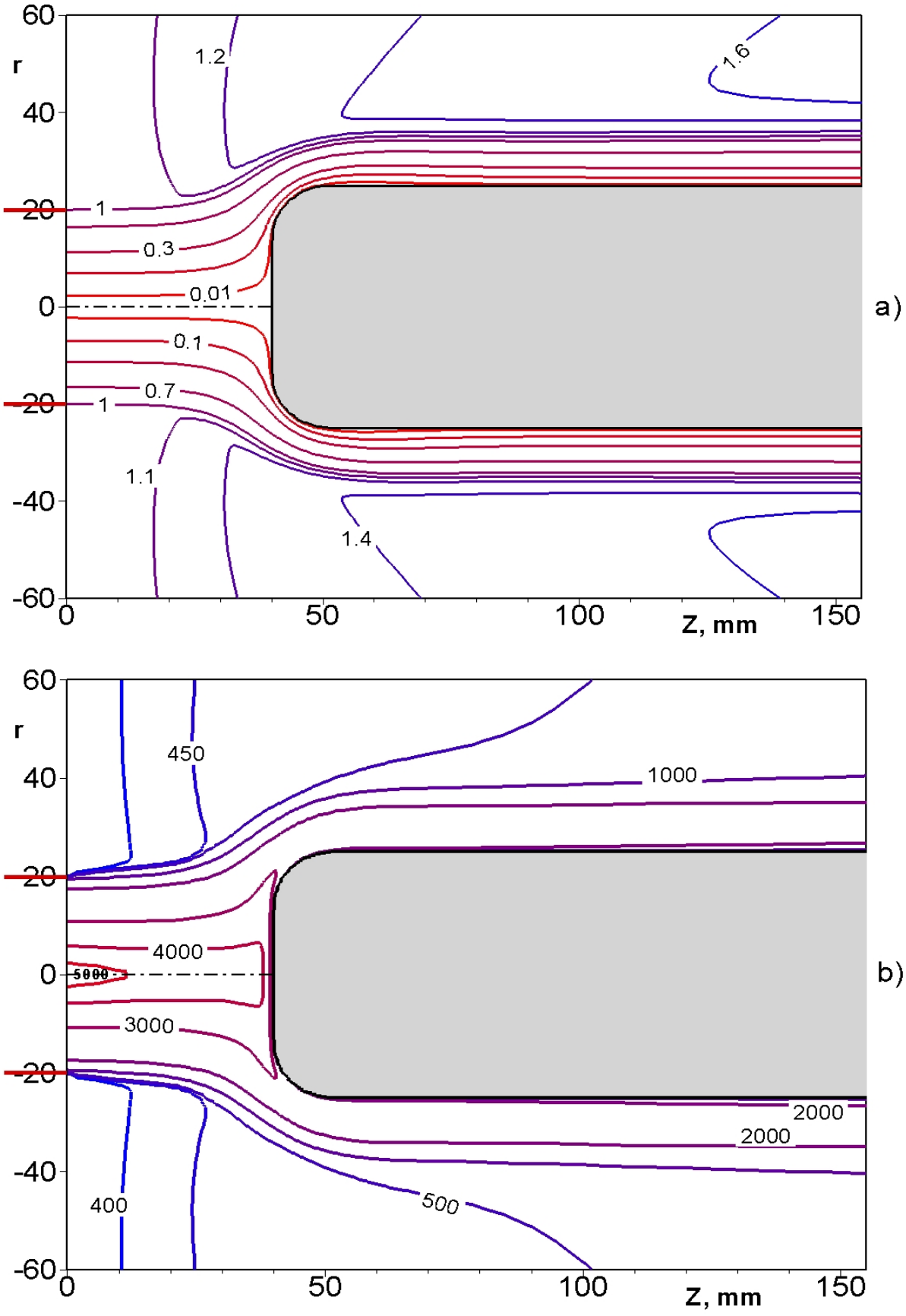

Figure 10: Streamlines (a) and isotherms (b) in the exhaust 97%CO_2+3%N_2 subsonic jet flow over euromodel, P=80 hPa, N_{pl}=20.28 kW, Zm=40mm.

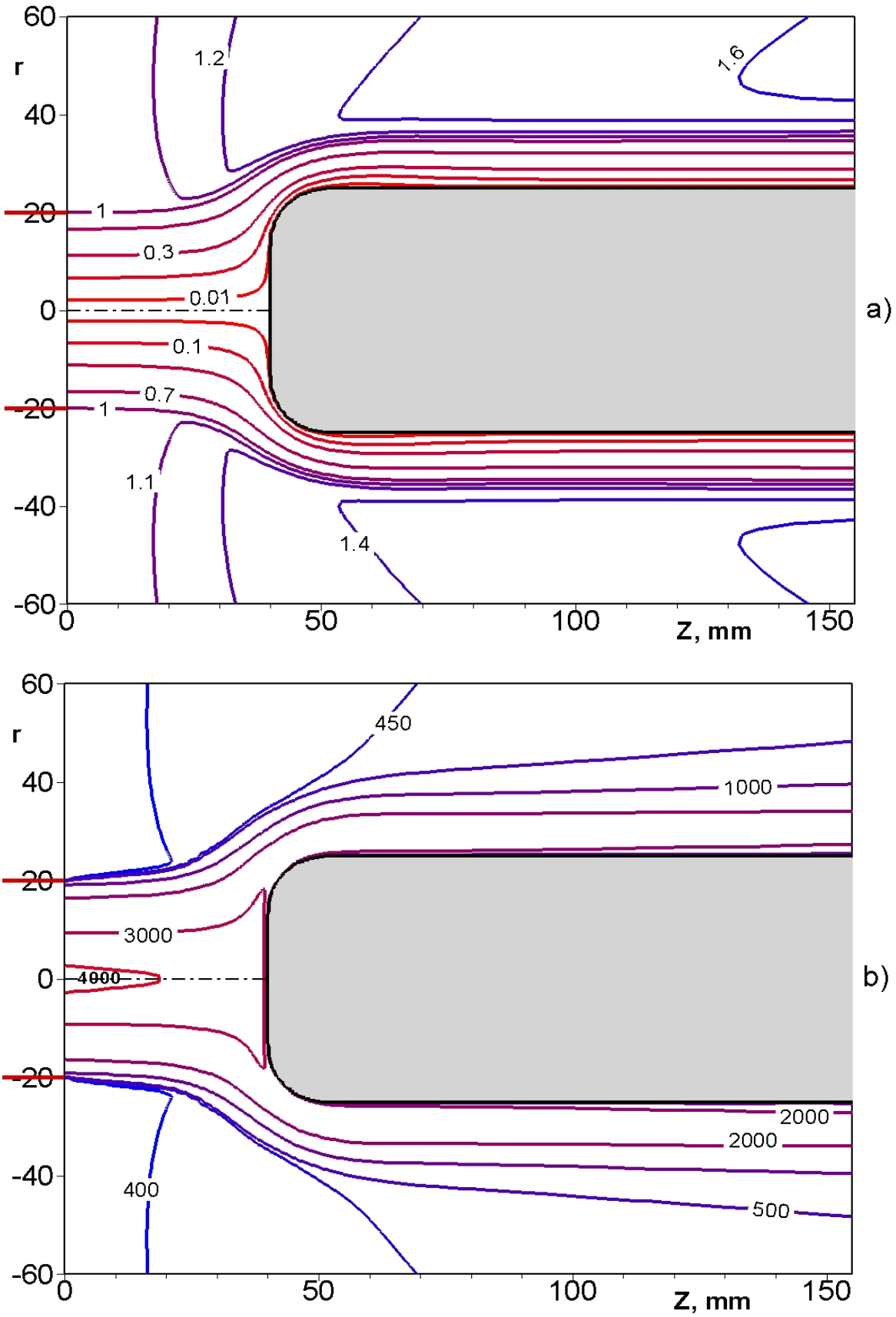

Figure 11: Streamlines (a) and isotherms (b) in the exhaust 97%CO_2+3%N_2 subsonic jet flow over euromodel, P=80 hPa, N_{pl}=16.45 kW, Zm=40mm.

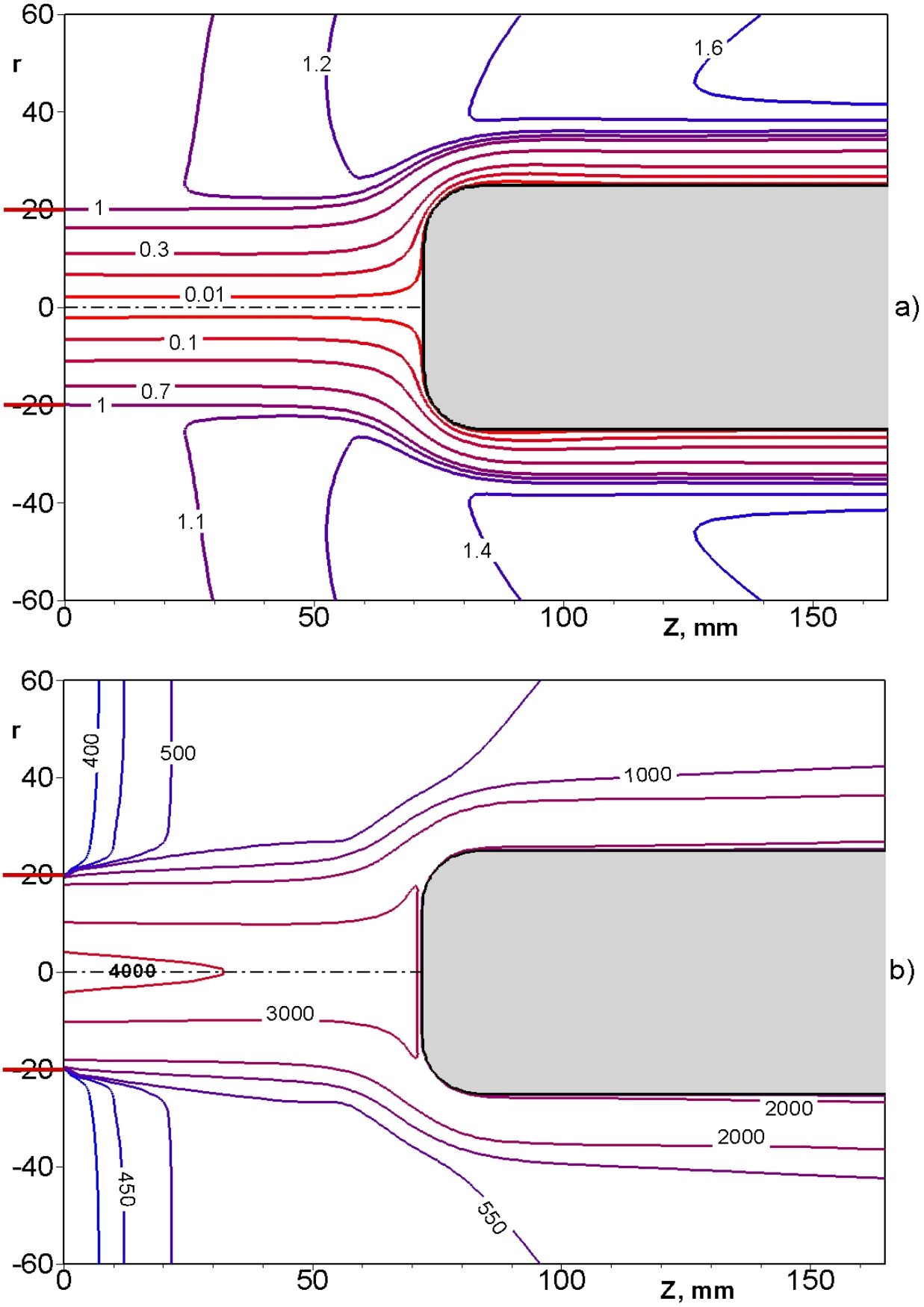

Figure 12: Streamlines (a) and isotherms (b) in the exhaust 97%CO_2+3%N_2 subsonic jet flow over euromodel, P=40 hPa, N_{pl}=17.05 kW, Zm=72mm.

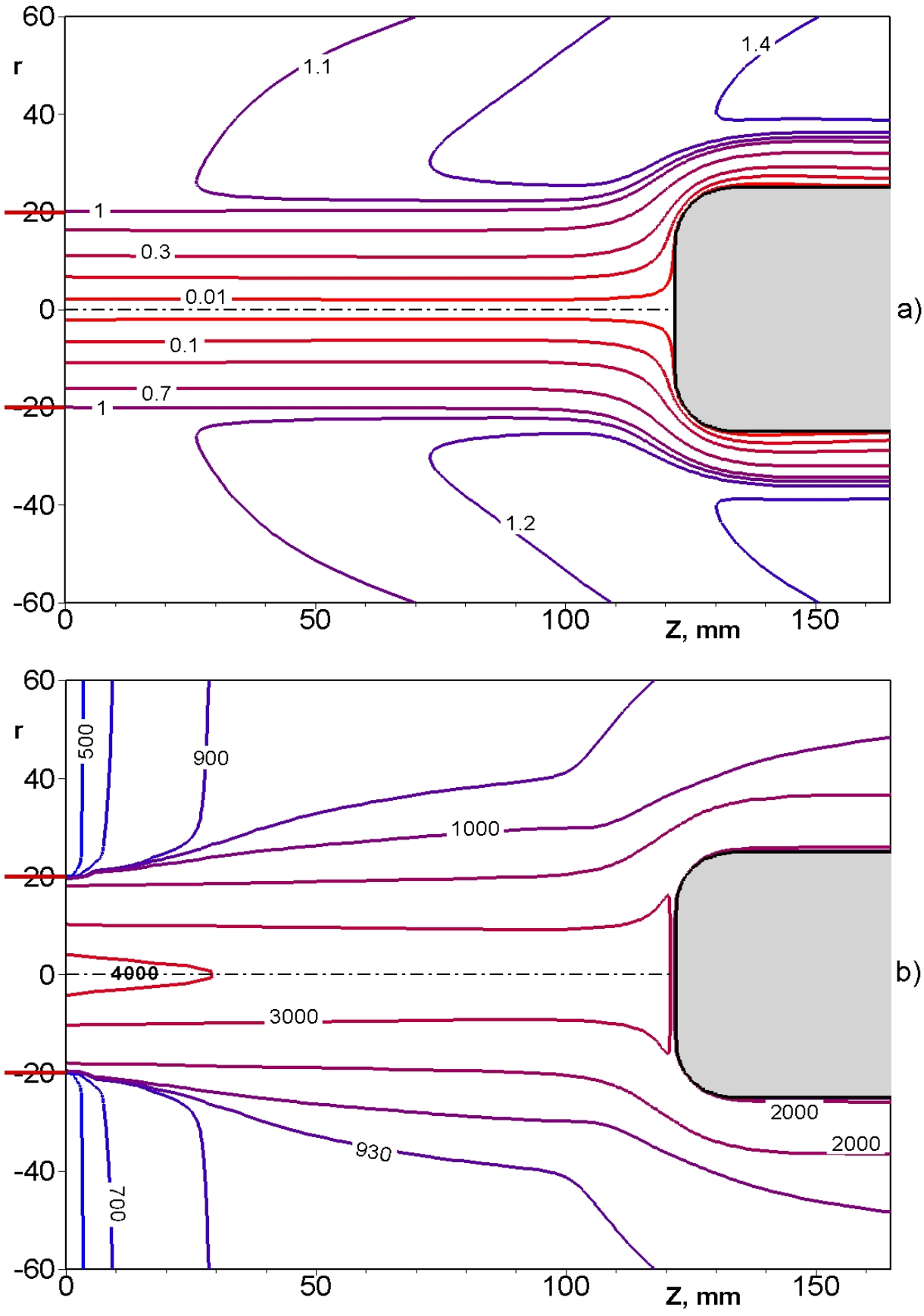

Figure 13: Streamlines (a) and isotherms (b) in the exhaust 97%CO_2+3%N_2 subsonic jet flow over euromodel, P=40 hPa, N_{pl}=17.05 kW, Zm=122mm.

Axial distributions of calculated plasma parameters from the torch exit to the model front surface are shown in Figs. 14-16: axial velocity u(z,0) [m/s] (Fig. 14), enthalpy h(z,0) [MJ/kg] (Fig. 15) and temperature T(z,0) [K] (Fig. 16). The notations on that Figures are analogous to that used in Chapter 3. The colored curves are the results obtained for 97%CO_2+3%N_2 flow for SACOMAR test regimes (Table 1), black dash curves are the results for the same regimes for pure CO_2 flow.

Analogous to the results at the channel exit section, one can see the difference between axial distributions calculated for 97%CO_2+3%N_2 and for pure CO_2 flow: maximum difference is about 1-2% for velocity and temperature profiles, and the enthalpy profiles are practically identical.

Figs. 17-18 show the dimensionless axial flow velocity u(z,0)/ u(0,0) and enthalpy h(z,0)/ h(0,0) for 97%CO_2+3%N_2 flow for SACOMAR test regimes. It is clear that the dimensionless parameters are more conservative: the dependence of dimensionless velocity on plasmatron power (N_{pl}=16.45 and 20.28 kW at P=80 hPa) is less than for the dimensional velocity. The dimensionless enthalpy results fall on the same line in the "free jet" region outside the boundary layer for corresponding Zm. On the other side, the dimensionless velocity axial distributions show the evident dependency on pressure for P=40 and 80 hPa. The corresponding results calculated for pure CO_2 flow are not shown in Figs. 17-18 because the dimensionless values are practically identical to the ones for 97%CO_2+3%N_2 flow.

Figs. 19 (a-d) show mole fractions X(i) of 8 components for equilibrium gas mixture (O, CO, O_2, N_2, CO_2, NO, N, C) calculated with Beta code along the jet axis, from the channel exit section to the outer edge of the boundary layer at the model, for the four test regimes. The mole fractions are presented in logarithmic scale. One can see that the mixture along the axis (outside the boundary layer near the model) consists mainly of the two leading components - O atoms and CO molecules. The concentrations of N2, NO, N components are about 1% or less, so the influence of 3%N_2 addition to the working gas is really negligible.

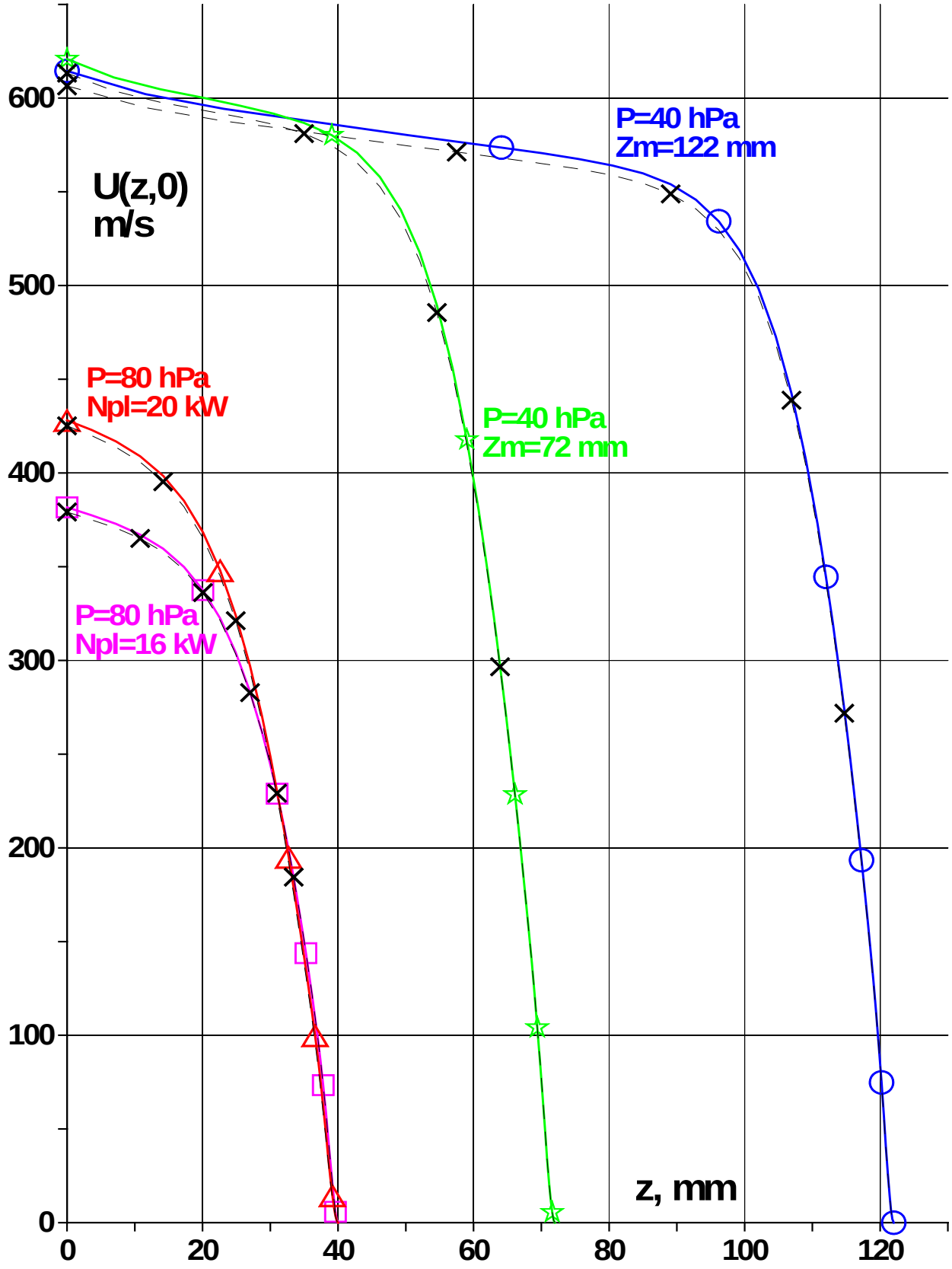

Figure 14: Velocity at the jet axis from the channel exit section to the model.

Colored curves are velocity at the jet axis for 97%CO_2+3%N_2 flow, black dash curves are the velocity for pure CO_2 flow. Blue curves & circles: P=40 hPa, Zm=122mm; green curves & stars: P=40hPa, Zm=72mm; red curves & triangles: P=80 hPa, N_{pl}=20.28 kW; magenta curves & squares: P=80 hPa, N_{pl}=16.45 kW.

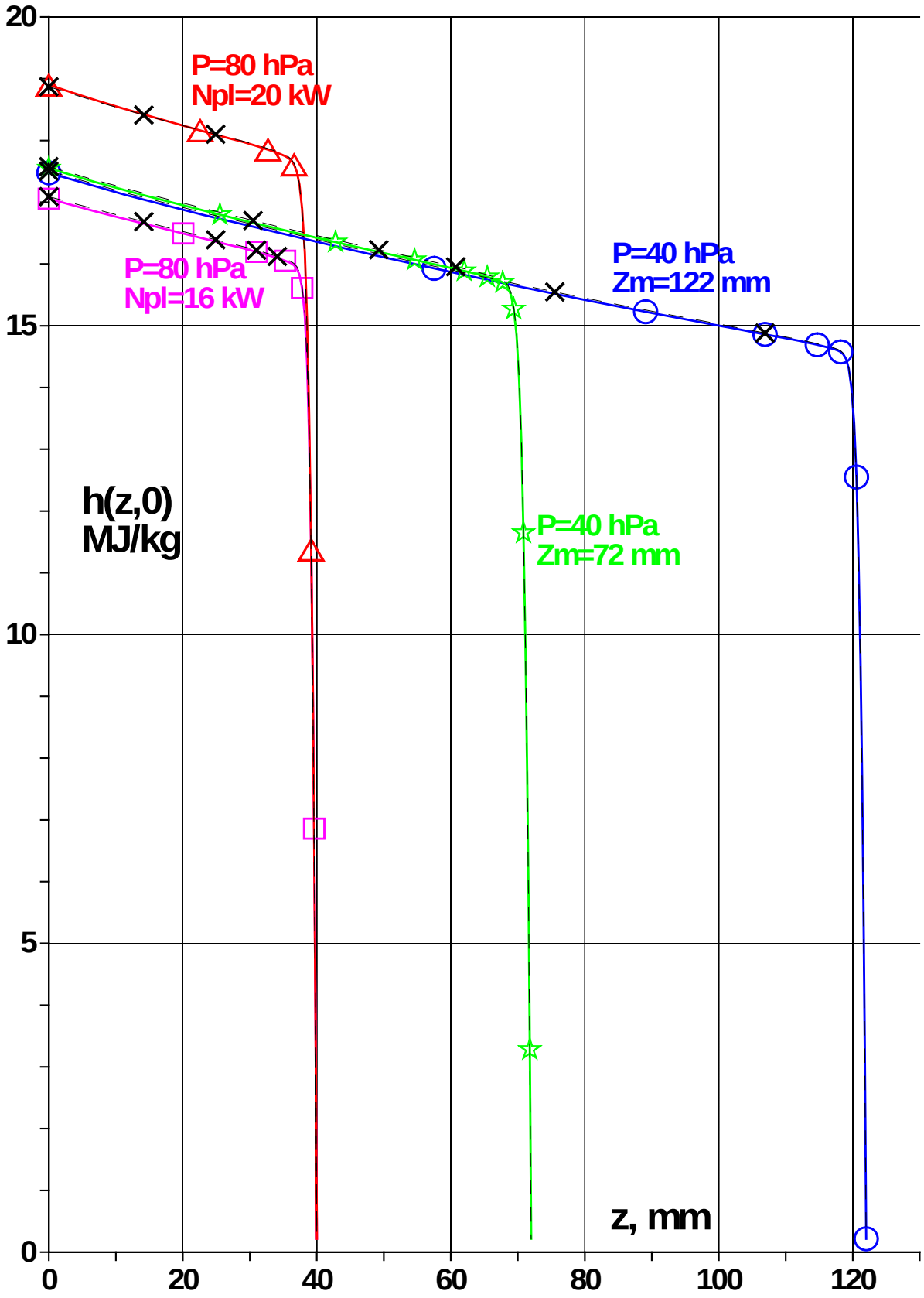

Figure 15: Enthalpy at the jet axis from the channel exit section to the model.

Colored curves are enthalpy at the jet axis for 97%CO_2+3%N_2 flow, black dash curves are the enthalpy for pure CO_2 flow. Blue curves & circles: P=40 hPa, Zm=122mm; green curves & stars: P=40hPa, Zm=72mm; red curves & triangles: P=80 hPa, N_{pl}=20.28 kW; magenta curves & squares: P=80 hPa, N_{pl}=16.45 kW.

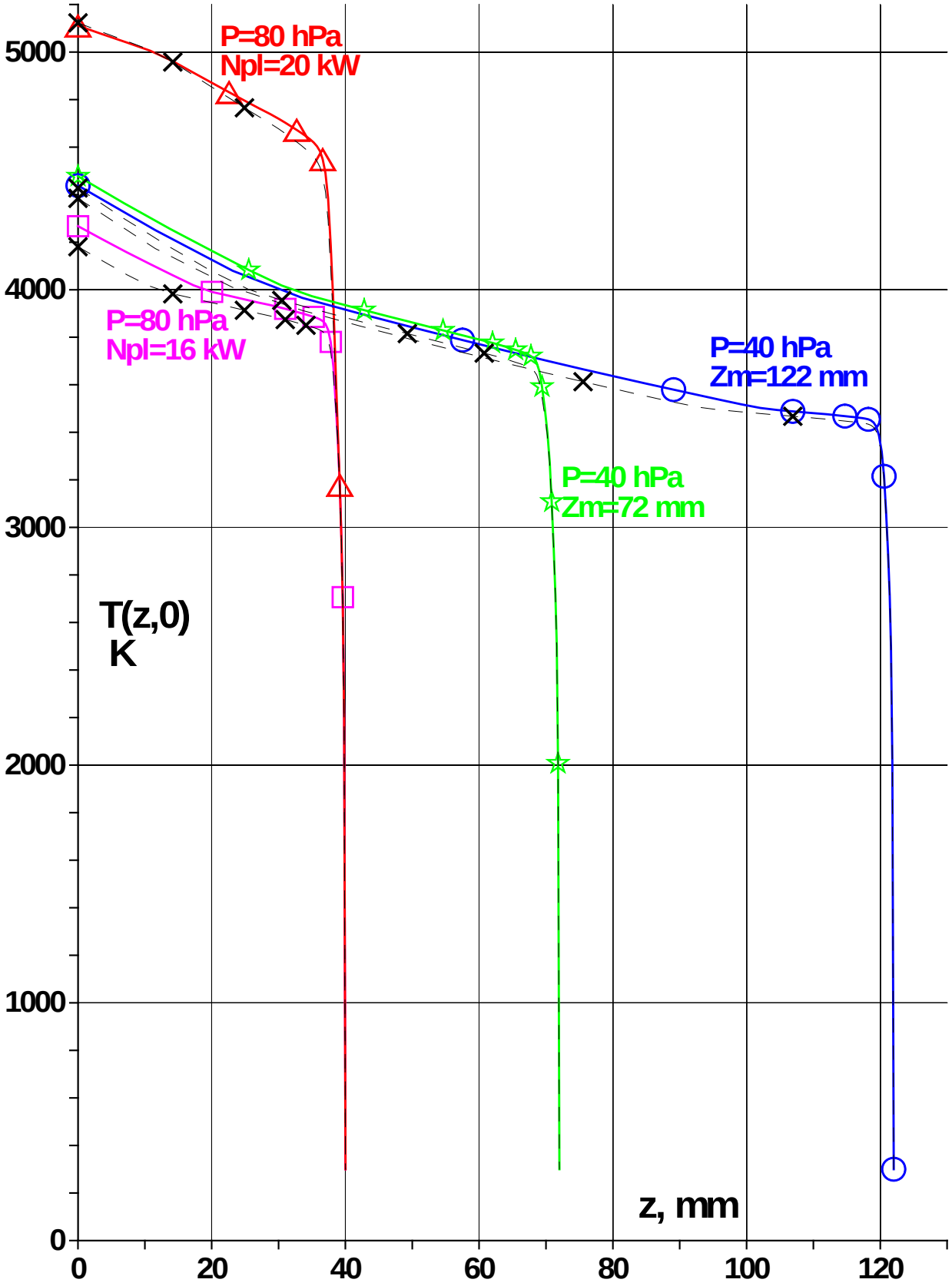

Figure 16: Temperature at the jet axis from the channel exit section to the model.

Colored curves are temperature at the jet axis for 97%CO_2+3%N_2 flow, black dash curves are the temperature for pure CO_2 flow. Blue curves & circles: P=40 hPa, Zm=122mm; green curves & stars: P=40hPa, Zm=72mm; red curves & triangles: P=80 hPa, N_{pl}=20.28 kW; magenta curves & squares: P=80 hPa, N_{pl}=16.45 kW.

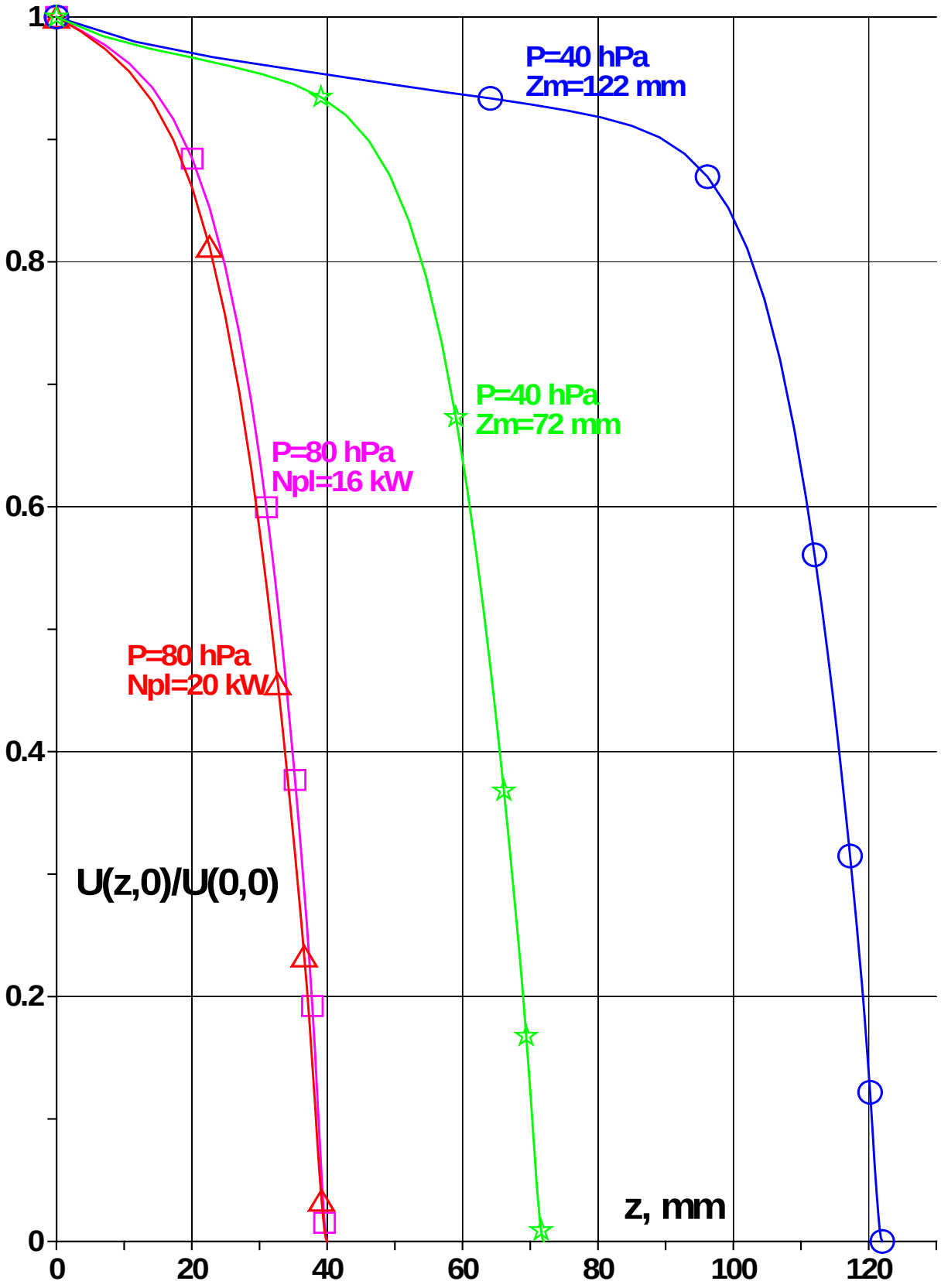

Figure 17: Dimensionless velocity along jet axis from channel exit section to the model.

Blue curves & circles: P=40 hPa, Zm=122mm; green curves & stars: P=40hPa, Zm=72mm; red curves & triangles: P=80 hPa, N_{pl}=20.28 kW; magenta curves & squares: P=80 hPa, N_{pl}=16.45 kW. All results presented here are for 97%CO_2+3%N_2 flows.

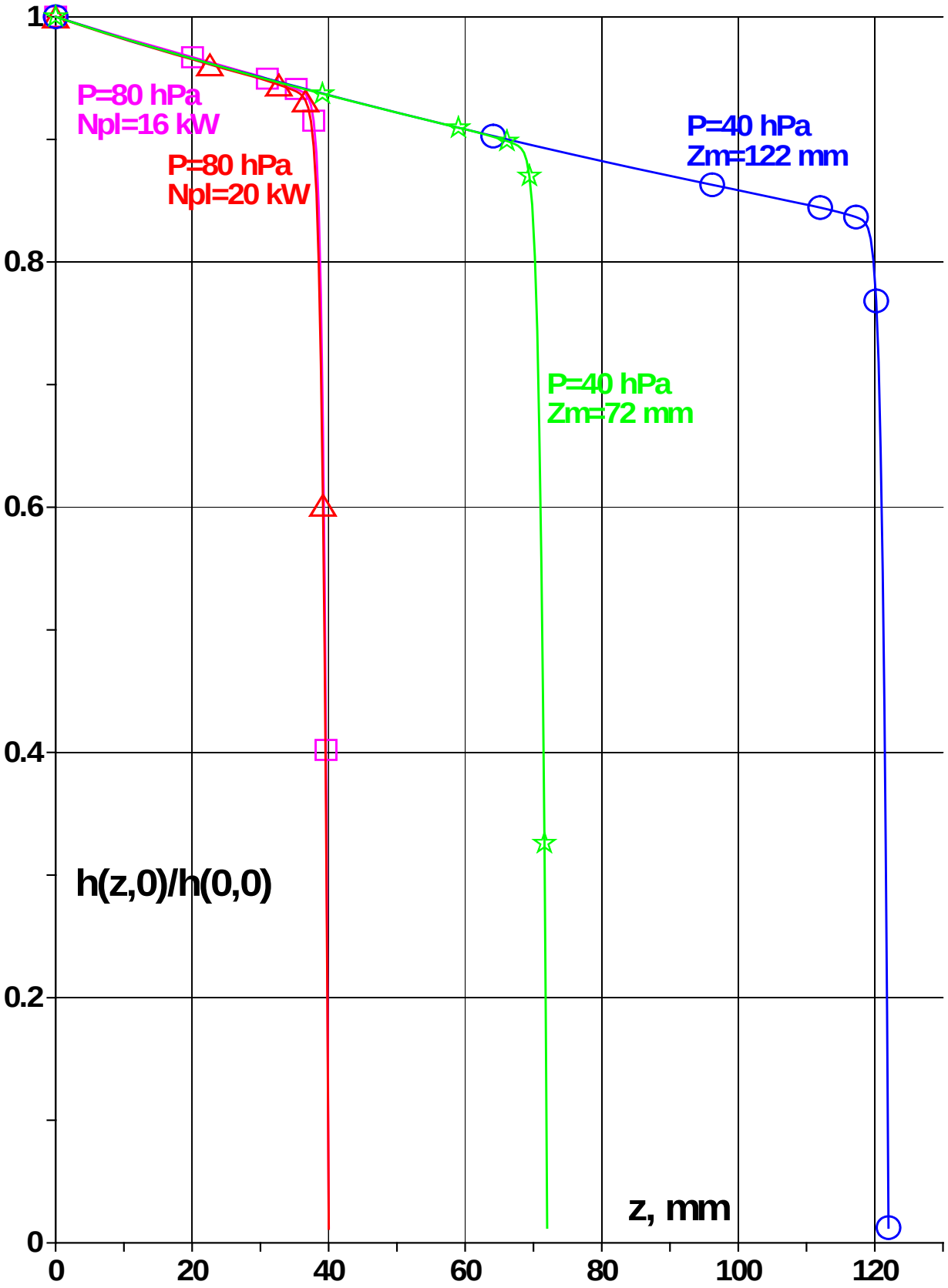

Figure 18: Dimensionless enthalpy along jet axis from channel exit section to the model.

Blue curves & circles: P=40 hPa, Zm=122mm; green curves & stars: P=40hPa, Zm=72mm; red curves & triangles: P=80 hPa, N_{pl}=20.28 kW; magenta curves & squares: P=80 hPa, N_{pl}=16.45 kW. All results presented here are for 97%CO_2+3%N_2 flows.

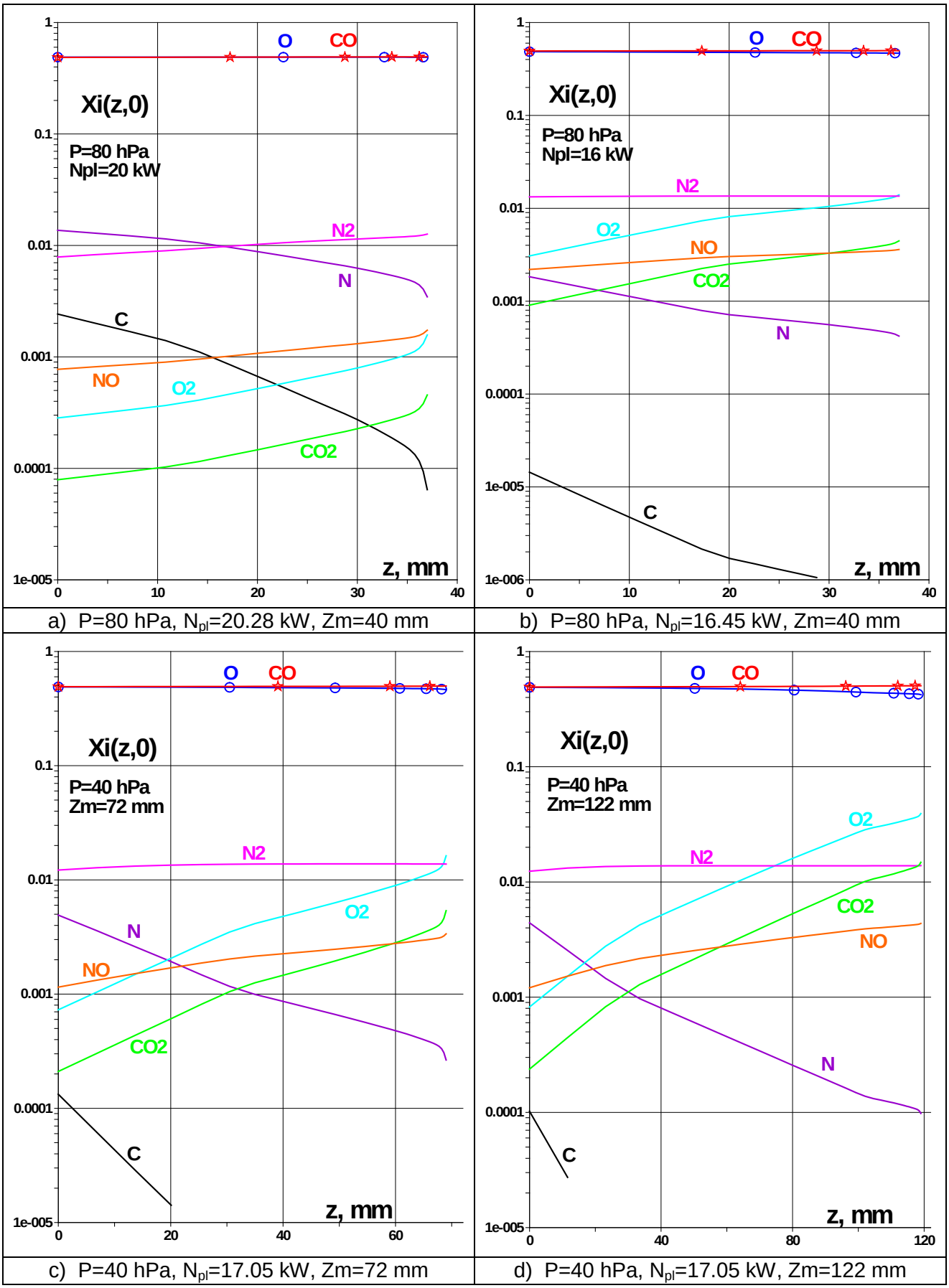

a) P=80 hPa, N_{pl}=20.28 kW, Zm=40 mm

b) P=80 hPa, N_{pl}=16.45 kW, Zm=40 mm

c) P=40 hPa, N_{pl}=17.05 kW, Zm=72 mm

d) P=40 hPa, N_{pl}=17.05 kW, Zm=122 mm

Figure 19: Mole fractions along the jet axis for the four test regimes.

The flow patterns in the discharge channel and plasma parameters at the channel exit section (Alpha results), distributions of jet flow parameters and gas mixture concentrations along the jet axis (Beta results) are valuable for apriori estimations that could be made before the experimental runs, and for analysis of high enthalpy jet parameters for the experimental conditions after the tests. But the accuracy of the dimensional flow parameters obtained from the CFD simulation could be not high due to the different reasons: the restrictions of the physical model used (LTE and laminar flow assumptions, absence of gas radiation, etc), use of simplified geometry of the inductor and test chamber, the inaccuracy of experimental data for N_{ap} and the plasmatron efficiency N_{pl}/N_{ap}, and some other reasons. For these reasons, the Beta code result for one of the key parameters - the jet flow enthalpy h_e - in general could be less accurate than the enthalpy rebuilt by Gamma code on the basis of the experimental measurements for heat flux q_{ws} to high catalytic material (silver for CO_2 flow) and dynamic pressure P_{dyn}.

In frameworks of IPM approach, the main result of Beta calculations is the set of dimensionless parameters that characterize the boundary layer thickness and flow vorticity in front of the model stagnation point. These dimensionless parameters are the necessary input data for the Gamma code. In fact they serve as the interface between the first stage of numerical simulation (Alpha and Beta codes) and the second stage (Gamma code). And final results such as the rebuilt enthalpy h_e, heat flux envelopes, recombination efficiency γ are obtained with use of Gamma code coupled with the corresponding experimental data.

The set of dimensionless parameters is defined by the jet flow parameters calculated with Beta code as follows:

Boundary layer thickness $\Delta=\delta/R_m$

Dimensionless parameters at the jet axis at the boundary layer external edge:

$\left(-\frac{V_e}{V_s}\right)$ - velocity at the boundary layer external edge V_e related to the reference velocity V_s;

$u_{1e}=\frac{R_m}{V_s}\left(\frac{\partial V_x}{\partial x}\right)_e$ - dimensionless velocity gradient;

$R_m\left(\frac{\partial u_1}{\partial y}\right)_e$ - second velocity derivative to determine the flow vorticity at the boundary layer external edge.

Here x and V_x are the coordinate along the model surface and the corresponding velocity component, u_1 is the velocity gradient near the get axis (these notations are used below in chapter 6 in the boundary layer equations):

$$u_1=u_1(x,y)=\frac{R_m}{V_s}\frac{\partial V_x}{\partial x}$$

u_{1e} is the velocity gradient at the jet axis (x=0) at the boundary layer external edge ($y=y_e$).

Note that the dimensionless parameters in question are very conservative in comparison with dimensional ones. Our previous numerical investigations [24] for air working gas showed that the dimensionless parameters change only in 3-6% when pressure is varied from 50 to 500 hPa, plasmatron power N_{pl} is varied from 12 to 36 kW, air flow rate G is varied from 2 to 5 g/s, on conditions that the plasmatron geometry is constant, including the geometry of the discharge channel, test chamber, testing model and the distance Zm from the channel exit section to the model.

5 Calculation of thermodynamic and transport properties of equilibrium plasmas

To calculate Navier-Stokes and Maxwell equations for Alpha code, and Navier-Stokes equations for Beta code, a set of thermodynamic and transport properties is necessary. These properties, including viscosity, thermal conductivity, electrical conductivity, can be calculated in advance for the case of chemical equilibrium mixture as functions of pressure and temperature.

We use here the standard assumptions:

- elementary composition of equilibrium mixture is constant (concentrations of chemical elements are constant); plasma is quasi neutral, $C_E^* = 0$;
- effects of non-ideal gas and plasma are not accounted;
- high frequency electromagnetic field does not influence the transport properties.

Special program package SoVA has been developed for calculation of chemical composition and transport properties of equilibrium multicomponent air and CO_2 plasma. In particular, transport properties of CO_2+N_2 plasma for the conditions of the test regimes were calculated by SoVA.

SoVA program package consists of the following two modules.

5.1 Calculation of chemical composition and thermodynamic properties

The first module was developed to calculate chemical composition of equilibrium CO_2 and air mixture of N=22 components produced by L=5 chemical elements (including the electron “e”):

O, N, C, Ar, e, O_2, N_2, CO_2, NO, CO,

O^+, N^+, C^+, Ar^+, O_2^+, N_2^+, CO_2^+, NO^+, CO^+, O^{++}, N^{++}, C^{++}.

This module provides calculations for the range of pressure and temperature: $0.001 \le P \le 10$ atm; $300 \le T \le 20000$ K, for "pure" gases (e.g. oxygen, nitrogen), and for gas mixtures such as air, CO_2 and CO_2+N_2 mixture.

Input data for this module are: pressure P, temperature T, mass fractions of chemical elements $C_j^*=C_{j\,0}^*$ (j=O, N, C, Ar) that generate a mixture.

Output data are:

- equilibrium mole fractions x_i,
- species molar enthalpies h_i (i=1,...N),
- heat capacities under constant pressure C_{pi} (i=1,...N),
- mixture molecular weight m,
- density ρ,
- specific enthalpy of a mixture h,
- specific heat capacity of a mixture under constant pressure C_p,
- reactions heat capacity C_{pr} calculated by the precise formula [25],
- effective (or total) heat capacity under constant pressure $C_{peff} = C_p + C_{pr}$ for equilibrium gas mixture.

To calculate equilibrium reaction rate constants K_{pr} and heat production Q_r, enthalpies h_i and heat capacities C_{pi} of species (i=1, ..., N), we use the approximations for the reduced Gibbs energy $\Phi_i(T)$ [26]. Here "r" is a reaction index, r=1, ..., R, R=N-L is the number of independent reactions

in the mixture. Additional approximations for O_2, N_2, CO_2 were developed for the low temperatures T<1000 K to calculate species heat capacities and enthalpies with higher accuracy. Additional approximations were used also for the second ions.

5.2 Calculation of transport coefficients

The second module was developed to calculate transport properties of multicomponent dissociated and partially ionized gas mixture, for the same pressure and temperature ranges as given above in 5.1.

Input data for the second module are: pressure, temperature and chemical composition of the mixture calculated by the first module.

Output data are transport coefficients for multicomponent gas mixture:

- viscosity $\mu(\xi)$;
- translational thermal conductivity $\lambda_{tr}(\zeta)$;
- thermal conductivity due to molecules internal energy transfer λ_{int};
- electrical conductivity $\sigma(\zeta)$;
- thermodiffusion ratios $K_{Ti}(\zeta)$ (i=1, ...N);
- "resistance coefficients" for multicomponent diffusion $\Delta_{ik}(\zeta)$ (i, k=1, ...N) used in the precise formula for $\lambda_R(\zeta)$ [27] ;
- thermal conductivity due to equilibrium chemical reactions $\lambda_R(\zeta)$;
- effective thermal conductivity $\lambda_{eff}(\zeta) = \lambda_{tr}(\zeta) + \lambda_{int} + \lambda_R(\zeta)$;
- effective Prandtl number $Pr_{eff} = C_{peff}\ \mu(\zeta) / \lambda_{eff}(\zeta)$;

Here ζ is the order of approximation by Sonine polynomials, i.e. number of terms in Sonine polynomial expansions of Boltzmann equation solution that provide convergence in Chapman-Enskog method, λ_{tr} is the “true” thermal conductivity corresponding to the following formula for the full heat flux [28]:

$$J_q = -\lambda_{tr} \nabla T + kT \sum_{i=1}^{N} \frac{K_{Ti}}{x_i} \frac{J_i}{m_i} + \sum_{i=1}^{N} h_i J_i$$

Where J_i is the mass diffusion flux for i-th species, k is the Boltzmann constant.

Calculations are made by the precise formulas of Chapman-Enskog method [28]. To calculate transport coefficients for neutral gases, the first non-zero approximation (ζ=1 for viscosity, ζ=2 for thermal conductivity) is rather accurate, but for ionized gas mixture this approximation can lead to error, up to ~50% error for air at T>15000 K when degree of ionization is high [27]. Therefore, our calculations for CO_2+N_2 plasma have been made with ζ=2 for viscosity, ζ=4 for other transport coefficients to provide high accuracy.

The formula from [28] used to calculate $\lambda_{tr}(\zeta)$, ζ=4, is presented below as an example:

$$\lambda_{tr}(4) = -\frac{75}{8} \frac{k\,n}{\det\|q\|} \times \begin{vmatrix} 0 & x_s & 0 & 0 \\ x_r & q_{rs}^{11} & q_{rs}^{12} & q_{rs}^{13} \\ 0 & q_{rs}^{21} & q_{rs}^{22} & q_{rs}^{23} \\ 0 & q_{rs}^{31} & q_{rs}^{32} & q_{rs}^{33} \end{vmatrix}, \quad \det\|q\| = \begin{vmatrix} q_{rs}^{11} & q_{rs}^{12} & q_{rs}^{13} \\ q_{rs}^{21} & q_{rs}^{22} & q_{rs}^{23} \\ q_{rs}^{31} & q_{rs}^{32} & q_{rs}^{33} \end{vmatrix} .$$

Here q_{rs}^{mp} – square matrixes of N × N order, their elements are expressed by the linear combinations of the collision integrals $\Omega_{ij}^{(l,s)}$ [29], $\det\|q\|$ – determinant of the order of 3N × 3N. Some details of the calculation technique and results obtained for air plasma had been presented in [27]. Note that the exploited formulas [28] for transport properties are essentially more convenient for calculations than the classic formulae [29-30] of Chapman-Enskog method, because the formulae from [29-30] are more complicated and they use the higher order determinants: Nζ×Nζ instead of N(ζ-1)×N(ζ-1).

To calculate transport coefficients, the collision integrals $\Omega_{ij}^{(l,s)}(T)$ are necessary. They are determined on the basis of the best available data on collision cross sections for various pairs of particles according to the recommendations [31].

As an example, calculated 97%CO_2+3%N_2 and pure CO_2 plasma transport coefficients are presented in Figs. 20, 21: effective thermal conductivity λ_{eff} [W/(m∗K)] and electrical conductivity σ [100/(Ohm∗m)]. Calculations are made by SoVA code at P=80 hPa with account for higher approximations, ξ=4. The results obtained for 97%CO_2+3%N_2 and pure CO_2 plasmas are practically identical for the viscosity and effective thermal conductivity. The electrical conductivity σ is also practically identical for 97%CO_2+3%N_2 and pure CO_2 plasmas in the high temperature range T ≥ 5000 - 6000 K. The essential difference in σ at lower T is explained by the relatively low ionization potential of NO, but this difference does not affect the plasma parameters at the discharge channel exit section because of the low values of σ (σ<0.01/Ohm/m) at lower T.

Tables of the necessary thermodynamic and transport properties for chemically equilibrium 97%CO_2+3%N_2 and pure CO_2 mixtures have been calculated with use of SoVA code to apply in Alpha and Beta codes.

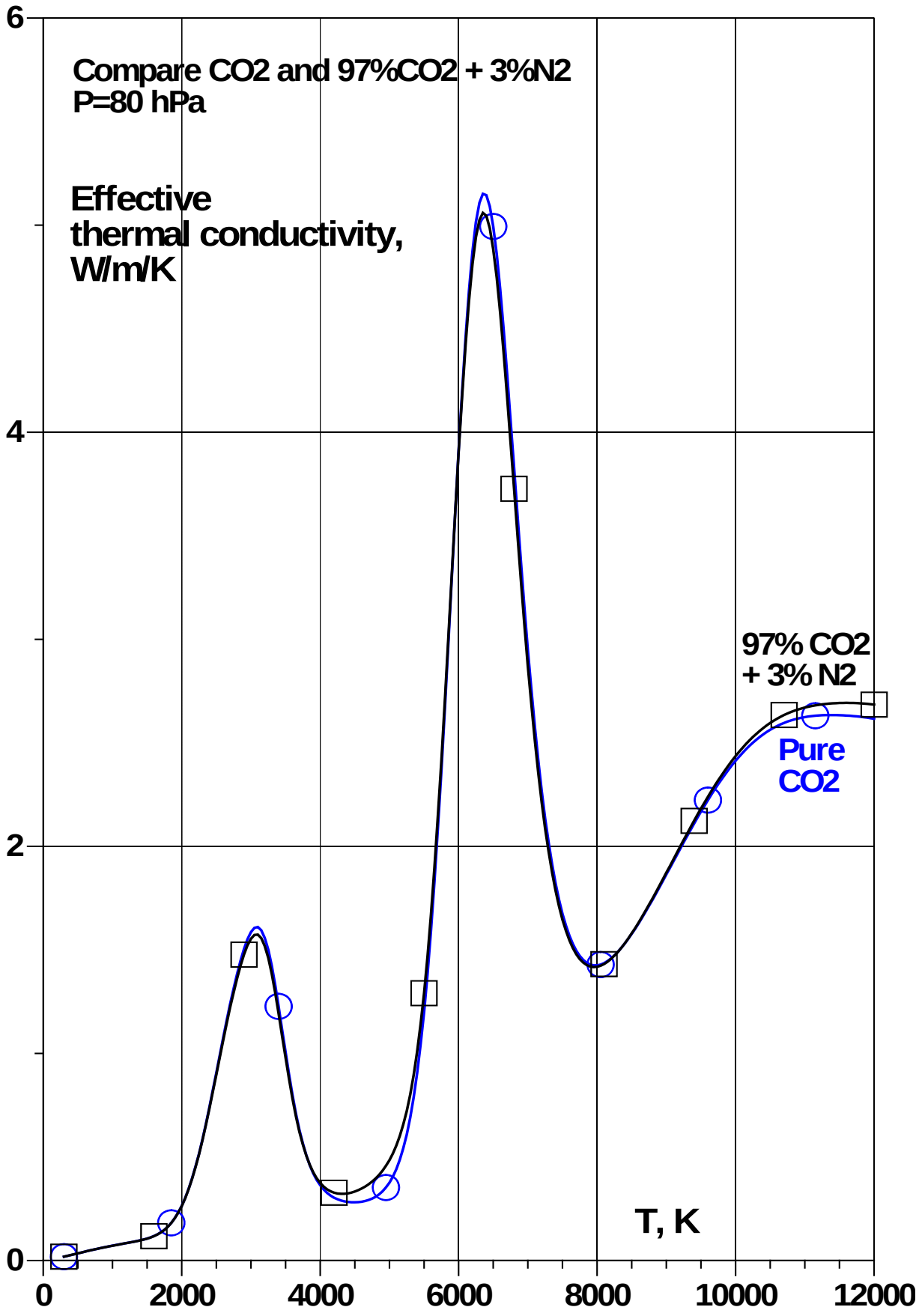

Figure 20: Effective thermal conductivity for 97%CO_2+3%N_2 and pure CO_2 at P=80 hPa.

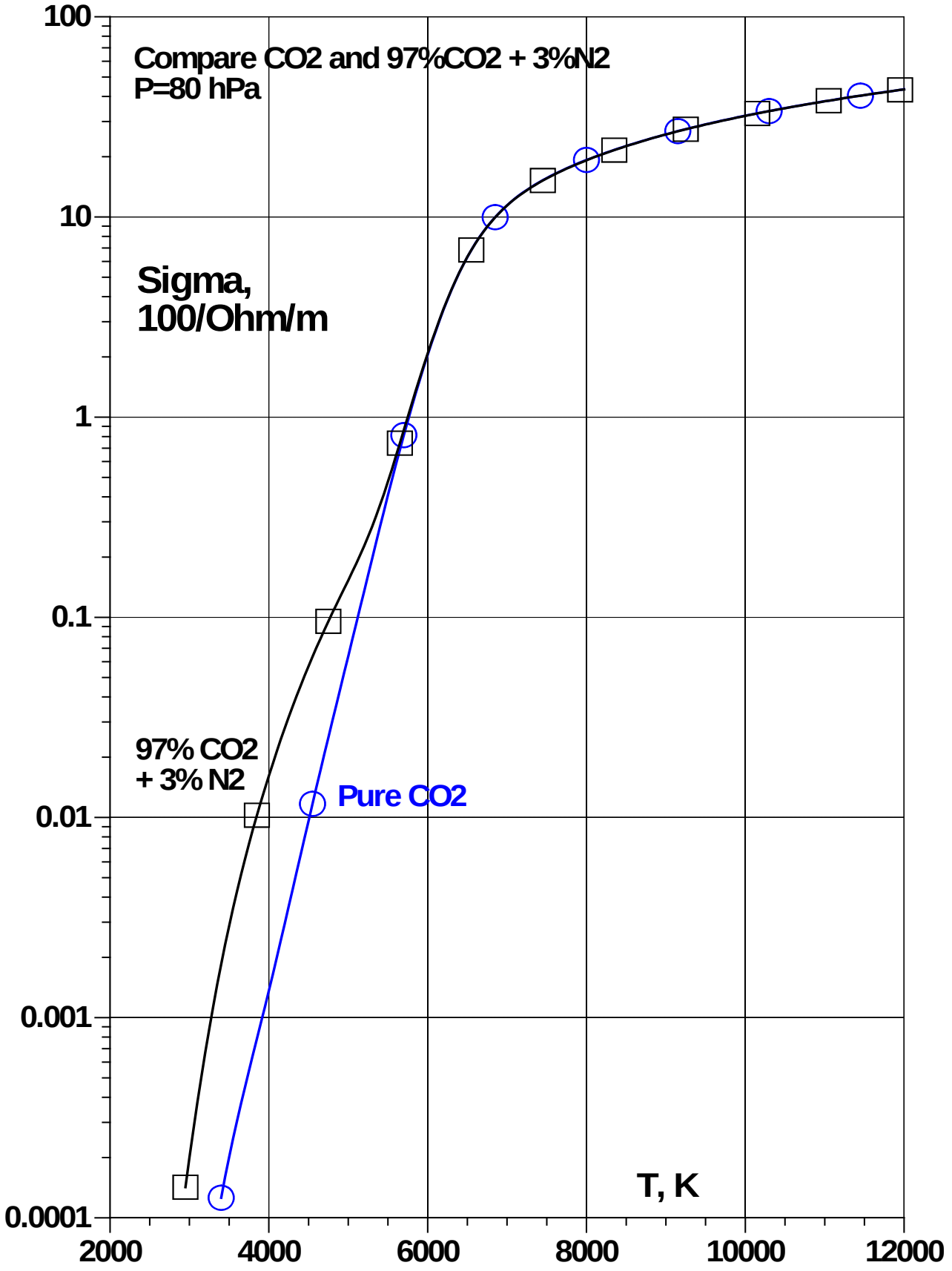

Figure 21: Electrical conductivity for 97%CO_2+3%N_2 and pure CO_2 plasma at P=80 hPa.

6 Calculation of boundary layer equations, determination of surface recombination efficiency

Problem formulation for the boundary layer equations with account for nonequilibrium chemical gas-phase reactions, finite thickness of the layer and flow vorticity at its external edge has been presented in our previous SACOMAR report [8], but for completeness we formulate here this problem with some additional details.

Numerical solution of the boundary layer equations is realized in Gamma code.

In spite of simplicity of Gamma code (it is based on 1D boundary equations), it is used exactly to provide the main results such as the rebuilt enthalpy h_e, heat flux envelopes, effective recombination coefficient γ. The reason is that Gamma code was developed so to be coupled with rather accurate experimental data, especially with the heat flux measurements.

The main features of IPM approach in calculation of the boundary layer equations and determination of the effective recombination coefficients for materials testing in dissociated CO_2 flow are the following [32].

♦ The flow enthalpy is rebuilt by the measured heat flux q_{ws} to the water-cooled calorimeter with oxidized silver surface, along with the rebuilding of reference velocity V_s by the P_{dyn} measured by Pitot tube. The details were presented in [8].

♦ The subsonic dissociated CO_2 jet flow is assumed to be equilibrium at the boundary layer external edge in front of the model, though the bulk boundary layer flow is under chemical non-equilibrium. This assumption helps to determine the species mass fractions C_{ie} at the boundary layer external edge by the known values of pressure P and enthalpy h_e. Temperature T_e is calculated along with enthalpy h_e from the flow equilibrium condition in the process of h_e rebuilding.

♦ The set of dimensionless parameters obtained previously with use of Beta code is used to provide the necessary input data for Gamma code in order to account for the boundary layer thickness and jet flow vorticity at the boundary layer external edge.

♦ Gas phase reaction rates are necessary to obtain the solution of nonequilibrium boundary layer equations. These rates are taken from [33].

♦ Appropriate model for catalytic surface recombination reactions should be used to provide boundary conditions for species diffusion mass flux at the model surface. The standard model of surface catalysis with use of the single effective parameter γ_w for all recombination reactions was used in IPM calculations [32]. This model was described in our previous SACOMAR report [34]. Also, the novel model was proposed in [34] with account for the EXOMARS entry conditions.

♦ Heat flux envelope $q_w=q_w(T_w, \gamma_w)$ is calculated with use of Gamma code on the basis of the above mentioned data and models.

♦ Value of γ_w for a testing material can be determined from the condition that the calculated heat flux is equal the measured one at the prescribed experimental conditions.

In application to the specified IPG-4 test regimes with 97%CO_2+3%N_2 flow, the above mentioned estimations are taken into account:

- maximum molar fractions of N_2 and N at the boundary layer external edge are about 1%, molar fractions of NO and other N-containing components are much lower;
- the difference of temperature and enthalpy calculated by Beta code for pure CO_2 and 97%CO_2+3%N_2 is about a few percents for different positions along the flow axis, e.g. at the discharge channel exit section and at the boundary layer external edge.

So, to simplify the problem formulation for the nonequilibrium boundary layer equations, we do not account for 3%N_2. Below the problem formulation is presented for the case of dissociated CO_2 mixture that consists of the 5 components: molecules CO_2, O_2, CO and atoms O and C.

In the next paragraphs the mathematical model of the nonequilibrium boundary layer equations is presented in dimensional and dimensionless forms. Further on, boundary conditions for the species diffusion flux at the wall are written for both the standard and the new surface catalysis models. Finally, numerical solution technique and computation results are presented.

Note that the third region (boundary layer at the symmetry axis in front of the model stagnation point) is essentially different from the first and second computational regions. So, some notations used in this chapter are different from the ones used before (i.e. the notations for coordinates and velocity components).

6.1 Model of flow and heat transfer in nonequilibrium boundary layer with finite thickness

Stationary axisymmetric laminar flow of dissociated gas mixture in the nonequilibrium boundary layer flow near the blunted model is considered. Cylindrical coordinate system (x, y) associated with the model flat face surface is shown in Fig. 22.

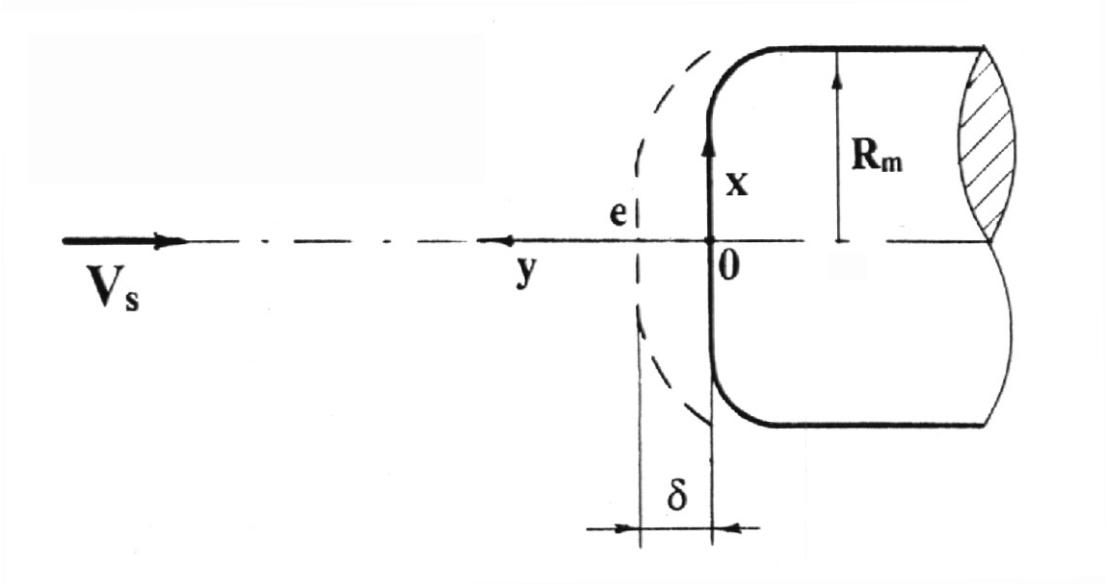

Figure 22: Schematic of jet flow and boundary layer near the model front face (the third computational region).

Flow in the boundary layer (it's thickness is $\delta \sim R_m\ Re^{-1/2}$) in the vicinity of the symmetry axis is governed with accuracy of $O(Re^{-1/2})$ by the following set of equations.

Equation of continuity:

$$\frac{\partial}{\partial x}\left(x\rho V_x\right)+\frac{\partial}{\partial y}\left(x\rho V_y\right)=0$$

Momentum equation (x-component):

$$\rho V_y \frac{\partial V_x}{\partial y} + \rho V_x \frac{\partial V_x}{\partial x} = -\frac{dP(x)}{dx} + \frac{\partial}{\partial y}\mu \frac{\partial}{\partial y} V_x$$

Energy equation written through the temperature:

$$\rho V_y C_p \frac{dT}{dy} + \sum_{i=1}^{5} J_i C_{pi} \frac{dT}{dy} = \frac{d}{dy}\frac{C_p}{\mathrm{Pr}}\frac{dT}{dy} - \sum_{i=1}^{5} h_i \dot{w}_i$$

Diffusion equations for mass concentrations of CO, C and O (i=3,4,5)

$$\rho V_y \frac{dC_i}{dy} = \frac{d}{dy}\frac{1}{Sc_i}\frac{dC_i}{dy} + \dot{w}_i$$

Here x and y are the coordinates related to the model surface, along and normal to the surface; V_x and V_y are the corresponding velocity components.

Equation of state:

$$P = \rho \frac{R_A}{m} T, \qquad \frac{1}{m} = \sum_{i=1}^{5} \frac{C_i}{m_i}$$

Conditions of mass conservation and conservation of chemical elements O and C are used to close the problem formulation.

The following gas-phase chemical reactions proceed in the dissociated CO_2 boundary layer flow:

$CO_2 + M \leftrightarrow CO + O + M$

$CO_2 + O \leftrightarrow CO + O_2$

$CO + M \leftrightarrow C + O + M$

$O_2 + M \leftrightarrow O + O + M$

$CO + O \leftrightarrow C + O_2$

($M = CO_2, O_2, CO, C, O$)

The data on rate constants for the gas-phase reactions were taken from [33].

Heat flux rate to the model stagnation point is determined by the formula:

$$q_w = -\left(\frac{C_p \mu}{\mathrm{Pr}}\right)_w \frac{dT}{dy} - \left(\frac{\mu}{Sc_O}\right)_w \frac{dC_O}{dy} h_O^0 - \left(\frac{\mu}{Sc_{CO}}\right)_w \frac{dC_{CO}}{dy} h_{CO}^0 - \left(\frac{\mu}{Sc_C}\right)_w \frac{dC_C}{dy} h_C^0$$

Here h_O^0, h_{NO}^0, h_N^0 are standard specific enthalpies of formation of O, CO, C.

6.2 Dimensionless governing equations

Stream function ψ (x, y) is determined by the relations:

$$\frac{\partial\psi}{\partial x} = -x\rho V_y, \qquad \frac{\partial\psi}{\partial y} = x\rho V_x$$

Dimensionless variables and parameters are determined as follows:

$$x' = x/R_m, \quad y' = y/R_m, \quad u = V_x/V_S\, x, \quad V = -V_y/V_S$$
$$\rho' = \rho/\rho_e, \quad T' = T/Te, \quad C'p = Cp/Cp_e, \quad C'p_i = Cp_i/Cp_e, \quad \mu' = \mu/\mu_e$$

Here R_m is the model radius, V_s is the reference velocity. All upper primes are omitted in further formulas. The new independent variable is determined:

$$\eta = 2\int_0^y \rho dy$$

Also, the dimensionless stream function f(η) is determined:

$$\Psi(x,y) = 0.5R_m^2\ \rho_e V_s x^2\ F(\eta_1), \quad F(\eta_1) = \rho V$$

Here gas parameters at the external edge of boundary layer are denoted by index "e".

Then the additional dimensionless variables are introduced - the dimensionless velocity gradient *u,* stream function *f* and independent variable η:

$$u = \frac{u_1}{u_{1e}}, \quad f = \frac{F}{\eta_{1e}u_{1e}}, \quad \eta = \eta_1/\eta_{1e}, \ 0 \le \eta \le 1$$

$$u_1 = u_1(x,y) = \frac{R_m}{V_s}\frac{\partial V_x}{\partial x}, \quad u_{1e} = u_1(x, y = y_e) = \frac{R_m}{V_s}\left(\frac{\partial V_x}{\partial x}\right)_e$$

$$\eta_{1e} = 2\int_0^\Delta \rho dy, \quad \eta_e = \eta_{1e}\sqrt{\frac{\mathrm{Re}\, u_{1e}}{2}} = \frac{\Delta}{\chi}\sqrt{2\,\mathrm{Re}\, u_{1e}}, \quad \mathrm{Re} = \frac{\rho_e V_s R_m}{\mu_e}, \quad \Delta = y_e = \delta/R_m$$

Finally a system of ordinary differential equations for boundary layer flow at the axis of symmetry (x=0) can be written with use of previously determined dimensionless variables:

$$\frac{d}{d\eta}\left(l\frac{du}{d\eta}\right) + f\frac{du}{d\eta} - \frac{1}{2}u^2 + \frac{1+\alpha_e}{2\rho} = 0, \quad u = \frac{df}{d\eta} \tag{13}$$

$$\frac{d}{d\eta}\left(\frac{lC_p}{Pr}\frac{dT}{d\eta}\right) + \sum_{i=1}^{5} C_{pi}\left(fC_i + \frac{l}{Sc_i}\frac{dC_i}{d\eta}\right)\frac{dT}{d\eta} - \sum_{i=1}^{5} h_i \dot{w}_i = 0 \tag{14}$$

$$\frac{d}{d\eta}\left(\frac{l}{Sc_i}\frac{dC_i}{d\eta}\right) + f\frac{dC_i}{d\eta} + \dot{w}_i = 0, \quad i = O,\ CO,\ C \tag{15}$$

The coefficients in these equations are determined as follows:

$$l = \frac{\rho\mu}{\eta_e^2}, \quad \frac{dy}{d\eta} = \frac{\Delta}{\rho\chi}, \quad \chi = \int_0^1 \frac{1}{\rho}d\eta, \quad \alpha_e = -\frac{V_e}{V_s}\frac{R_m}{u_{1e}^2}\left(\frac{\partial u_1}{\partial y}\right)_e$$

Here α_e is the parameter to account for the external flow vorticity, C_{pi} and C_p are the specific heats of i-th species and gas mixture, Pr is the mixture Prandtl number, Sc_i is the Schmidt number of i-th

species, h_i is the enthalpy of i-th species, $\dot{w}_i$ is the source term for i-th species production in the gas-phase reactions.

Additional equations to close the system are:

$$\frac{1}{\rho} = \frac{T}{m}, \quad h = \sum_{i=1}^{5} C_i h_i ,$$

Boundary conditions at external edge of boundary layer (η=1) are:

$u = T = 1, \quad C_i = C_{ie}$

Boundary conditions at the surface (η=0) are:

$u = f = y = 0, \quad T = T_w/T_e$

Boundary conditions at the surface for dimensionless diffusion fluxes will be determined below.

To provide data for boundary conditions and for the coefficients of the boundary layer equations, the following input data are used:

- Pressure P, reference velocity V_s, flow temperature T_e and species concentrations C_{ie} at the boundary layer external edge.
- The set of dimensionless parameters calculated in advance by Beta code.

6.3 Models of catalytic surface recombination reactions

Standard model of surface catalysis

Boundary conditions at the surface for diffusion fluxes for the standard model of surface catalysis (Goulard's type) are the following (dimensional form).

$$-J_{CO} = \rho K_{WCO} c_{CO} \tag{16}$$

$$-J_{O} = \rho K_{WO} c_{O} \tag{17}$$

$$-J_{C} = \rho K_{WC} c_{C} \tag{18}$$

Here J_i is the diffusion mass flux for i-th species, all parameters here refer to the flow at the surface, the index "w" is omitted. Note that the catalytic recombination of C atoms gives a small input to the total heat flux for the specified IPG-4 test conditions due to the very small concentration of C atoms in boundary layer. So, the third condition (for J_c) is formal one, actually we can use

$$J_C = 0 \tag{19}$$

instead of (18), and the effective value γ_w describes the effective surface recombination of O atoms and CO molecules.

Here the reactions of surface recombination of O and C atoms and CO molecules are assumed to be of the first order. The catalytic recombination rates K_{wi} are expressed through the effective recombination coefficients γ_{wi}:

$$K_{Wi} = \frac{2\,\gamma_{wi}}{2 - \gamma_{wi}} \sqrt{\frac{R_A T_W}{2\,\pi\, m_i}} \tag{20}$$

The key assumption of the standard model is the use of effective coefficient γ_w to describe in total the effect of all catalytic reactions: $\gamma_w = \gamma_{wO} = \gamma_{wCO} = \gamma_{wC}$. In this way we introduce the average efficiency of recombination γ_w. The reason for this simplification is that we have only one measured parameter q_W to rebuild the surface catalycity.

To close the problem formulation, it is necessary to use the additional boundary condition of O atoms balance on the surface:

$$J_{O_2} + \frac{2m_O}{m_{CO_2}} J_{CO_2} + \frac{m_O}{m_{CO}} J_{CO} + J_O = 0 \tag{21}$$

Two-parameter model of surface catalysis based on Eley-Rideal mechanism

The previous single-parameter model is modified according [35] on the bases of the theory of Langmuir ideal adsorbing layer for Eley-Rideal mechanism, which dominates on cold walls. Then we have boundary conditions with the two recombination rates K_{WO} and K_{WCO} as follows [34]:

$$-J_O = \rho K_{WO} c_O + \frac{m_O}{m_{CO}} \rho K_{WCO} c_{CO} \tag{22}$$

$$-J_{CO} = \rho K_{WCO} c_{CO} \tag{23}$$

$$J_C = 0 \tag{24}$$

and equation (21) is used also to close the problem formulation. Here again all parameters refer to the flow at the surface, the index "w" is omitted.

In this new two-parameter model, when the catalytic recombination rate K_{wO} depends only on surface temperature, it can be taken from the literature data for pure atomic oxygen recombination and in that case the second recombination rate K_{wCO} can be rebuilt from heat flux measurements in CO_2 plasma flows.

The catalytic recombination rates K_{wO}, K_{wCO} can be expressed through the effective recombination coefficients γ_{wO}, γ_{wCO} by the same equation (20).

6.4 Numerical solution technique and computation results

The Gamma code was developed to realize numerical solution of the dimensionless nonequilibrium boundary layer equations along the flow axis from the boundary layer external edge to the model surface with account for finite layer thickness at low Re and surface catalycity. It provides the rebuilding of flow enthalpy h_e at the external boundary layer edge and calculation of heat flux q_w (T_w, γ_w) in the model stagnation point as function of both the surface temperature T_w and effective recombination coefficient γ_w (heat flux envelope).

Finite difference scheme [36] is used to solve the one-dimensional boundary value problem for the governing equations (13)-(15). This scheme provides the 4-th order of approximation by η coordinate and good monotonous properties. The system of equations (13)-(15) together with equation of state and other additional algebraic equations is solved by cascade iterations. The under-relaxation technique is used to provide the convergence. This numerical method provides calculations up to P=1 atm, i.e. up to near-equilibrium regimes.

Normally about 20 grid points are used across the boundary layer to provide 1% accuracy. Test calculations with variable number of grid points NK, up to NK=300, prove fast convergence and accuracy of solution.

It takes a few seconds to rebuild the flow enthalpy and calculate the heat flux envelope for one typical IPG-4 regime by GAMMA code.

Below the Figs. 23-26 present comparison of heat flux envelopes calculated by the standard model (16)-(18) and the novel model (22)-(24) of surface recombination for the specified IPG-4 test regimes (Table 1). The novel model (22)-(24) is the two parameter one, but for the comparison here we used assumption $\gamma_w = \gamma_{wO} = \gamma_{wCO}$ in the novel model. Even for this case the novel model differs from the standard one due to the extra "non-diagonal" term in (22).

In addition, the extra regime with higher plasmatron power (N_{ap}=45 kW) and enthalpy (h_e=17.5 MJ/kg) was calculated just to demonstrate the novel model of surface recombination at higher enthalpy. This IPG-4 regime was actually realized at the stage of enthalpy rebuilding and determination of the test regimes with h_e values specified by SACOMAR test matrix, see [8]. Heat flux envelopes for both the standard and the novel model of surface recombination for the extra regime P=80 hPa, N_{ap}=45 kW are presented in Fig. 27.

The notations for the Figs. 23-27:

1) Boundary curves:

- upper red dash-dotted curve denotes the heat flux to fully catalytic wall,
- lower blue dash-dotted curve denotes the heat flux to non-catalytic wall,
- bottom cyan dash-dotted curve denotes the heat flux to non-catalytic wall calculated for the frozen flow (without gas-phase reactions).

2) Internal curves:

- solid curves with stars denote the heat flux calculated by the novel model (22)-(24),
- dash curves denote the heat flux calculated by the standard model (16)-(18).

Note that the boundary curves actually are not related with the standard or the novel model, because they present the results obtained with the corresponding limit cases:

- The model of fully catalytic wall can be expressed with the boundary conditions at the wall

$$C_{wO} = C_{wCO} = C_{wC} = 0 \qquad (25)$$

In fact calculations by the standard model (16)-(18) for the case $\gamma_w = 1$ provide the results practically identical to the ones obtained with (25) boundary conditions.

- The case of non-catalytic wall can be expressed with the boundary conditions at the wall

$$J_{wO} = J_{wCO} = J_{wC} = 0 \qquad (26)$$

Obviously calculations by the standard or by the novel models with $\gamma_w = 0$ provide the results identical to the ones obtained with (26).

Numerical investigation and analysis of physical meaning of the novel model of surface recombination (22)-(24) revealed that the use of this model is limiting by the following condition: concentration of oxygen atoms in gas flow at the wall should be high enough to provide the possibility of surface recombination for the CO molecules defined by the corresponding recombination efficiency γ_{wCO} (or by the recombination rate K_{WCO}). This limiting condition is related with extra "non-diagonal" term in (22). When concentration of O atoms in boundary layer is low and the formulated condition is not provided, the model (22)-(24) is not applicable. In numerical calculations the inapplicability of the model is manifested in negative concentration of O atoms that appears in one point or in a few grid points near the wall.

Limits of application of the novel model are determined first of all by the test conditions - flow enthalpy h_e and pressure P, and also by the value of γ_w, and sometimes even by the surface temperature T_w: see Fig. 26, the heat flux curve q_w (T_w, γ_w=0.01) calculated by the novel model is started at T_w=800 K, because calculations by the novel model for T_w=300÷700 K showed the appearance of negative C_O values at the wall.

In numerical calculations we determined the applicability condition for the novel model as the absence of negative concentrations C_O in boundary layer flow.

Calculations for the four IPG-4 test conditions (see Table 1) revealed the following upper limits γ_{wLimit} for the novel model:

P=80 hPa, N_{ap}=40.4 kW, Zm=40 mm: $\gamma_{wLimit} \approx 0.01$

P=80 hPa, N_{ap}=34.0 kW, Zm=40 mm: $\gamma_{wLimit} \approx 0.0032$

P=40 hPa, N_{ap}=35.0 kW, Zm=72 mm: $\gamma_{wLimit} \approx 0.032$

P=40 hPa, N_{ap}=35.0 kW, Zm=122 mm: $\gamma_{wLimit} \approx 0.01$

Calculation for the extra regime with higher plasmatron power and flow enthalpy, P=80 hPa, N_{ap}=45 kW, h_e=17.5 MJ/kg (Fig. 27), revealed no limitations for the novel model, because concentration of O atoms in the boundary layer is high enough for this case.

Remember that in these calculations we used equal values $\gamma_w = \gamma_{wO} = \gamma_{wCO}$ in the novel model just to compare it with the standard one.

In Figs. 23-27 the heat flux values q_w (T_w, γ_w) calculated by the novel model for $\gamma_{wLimit} \geq \gamma_w > 0$ are always higher than that calculated by the standard model. Consequently, values of recombination coefficient γ_w and recombination rate K_W obtained with the novel model will be lower. The difference is appreciable for values of γ_w far from the limiting ones (0 and 1), and decreases when γ_w values are close to the limits (Fig. 27).

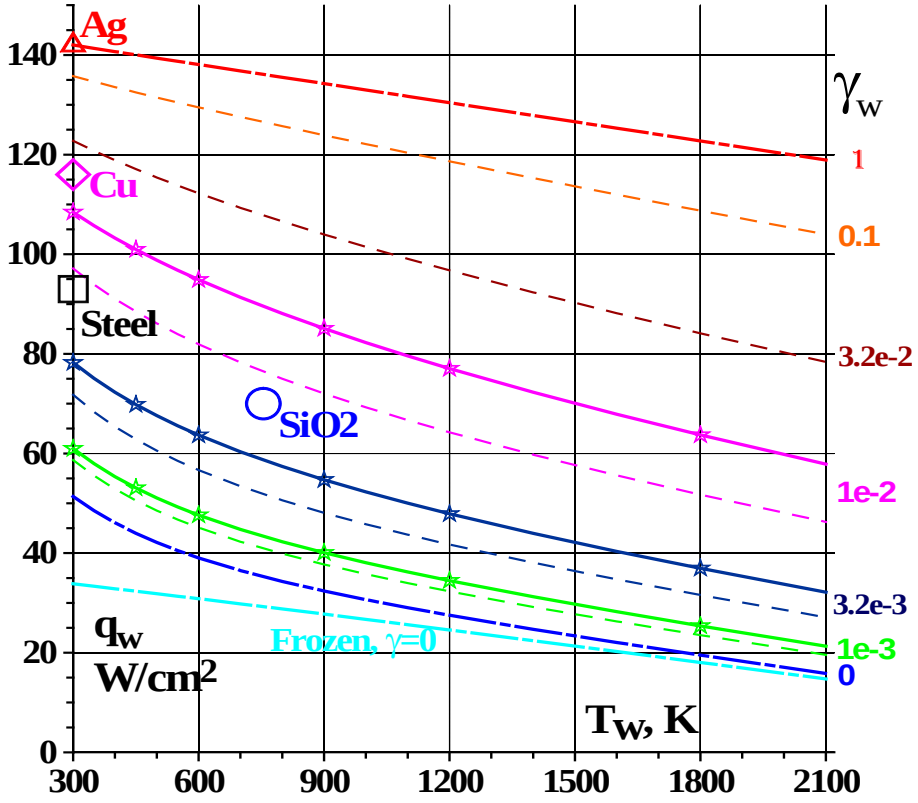

Figure 23: Heat flux envelopes for standard and novel surface catalysis models for test regime: P=80 hPa, N_{ap}=40.4 kW.

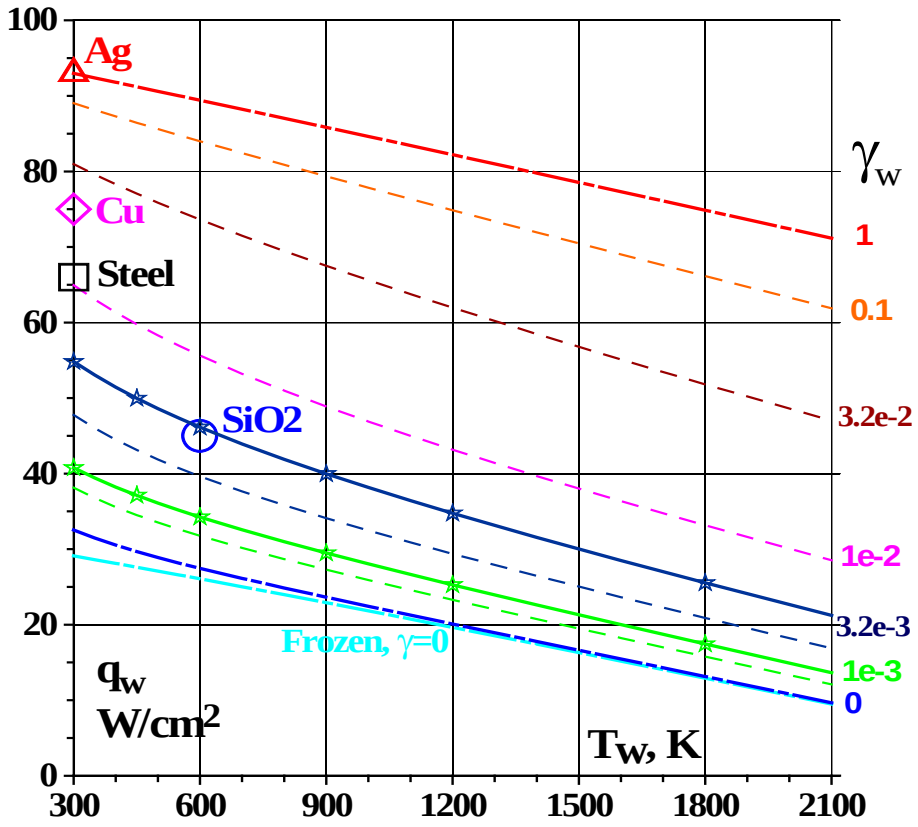

Figure 24: Heat flux envelopes for standard and novel surface catalysis models for test regime: P=80 hPa, N_{ap}=34 kW.

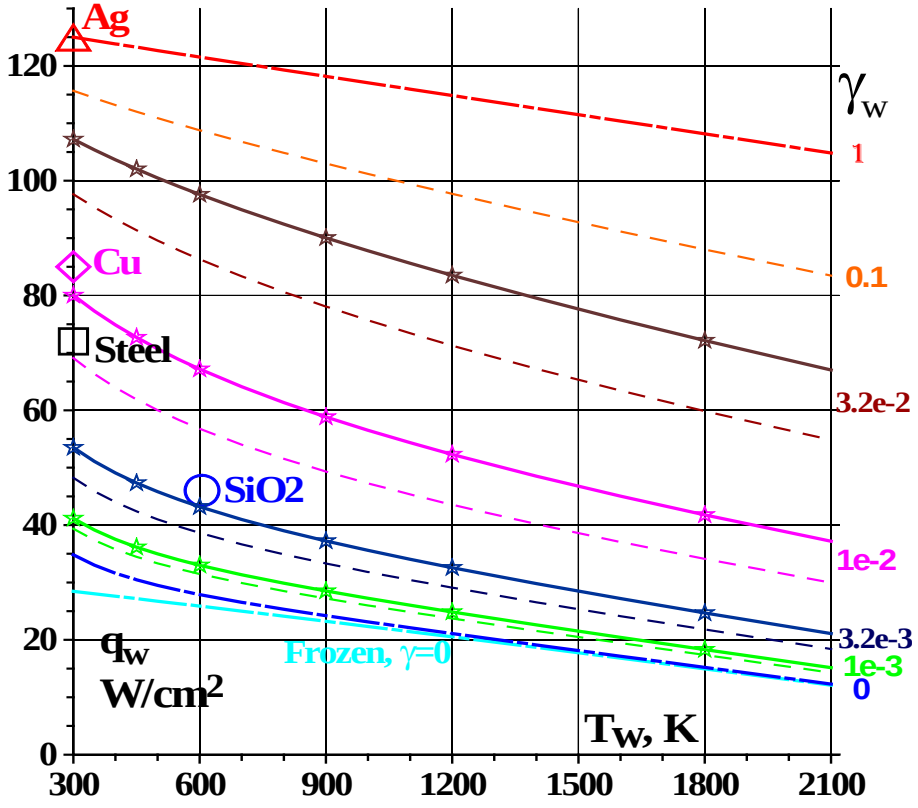

Figure 25: Heat flux envelopes for standard and novel surface catalysis models for test regime: P=40 hPa, Zm=72 mm.

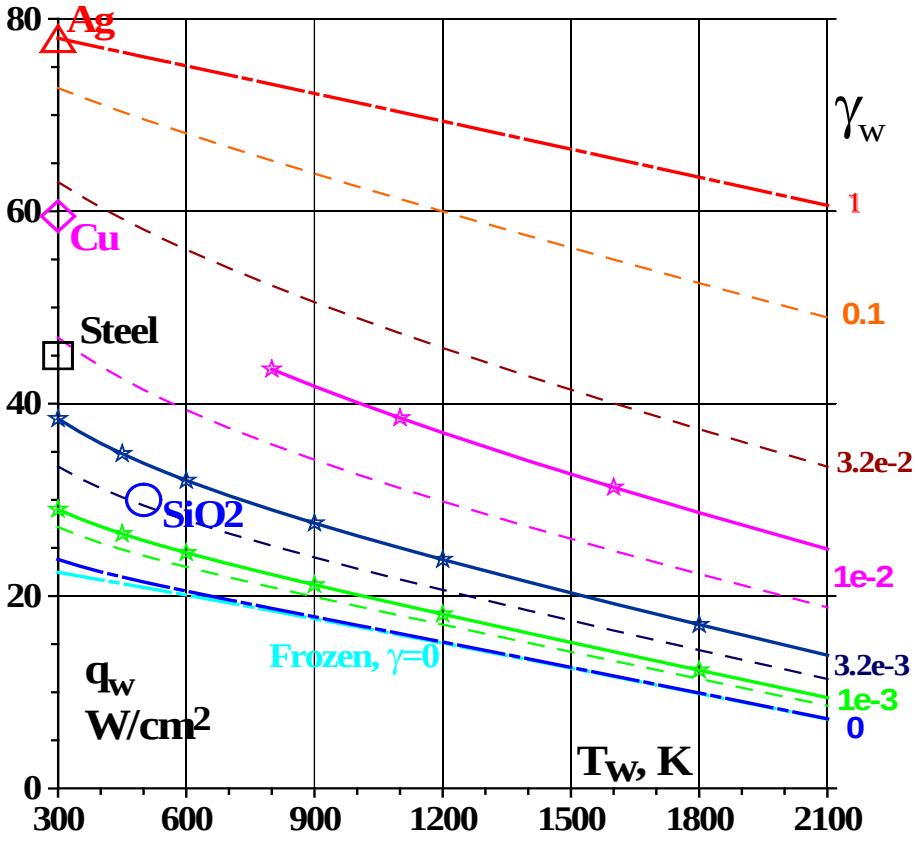

Figure 26: Heat flux envelopes for standard and novel surface catalysis models for test regime: P=40 hPa, Zm=122 mm.

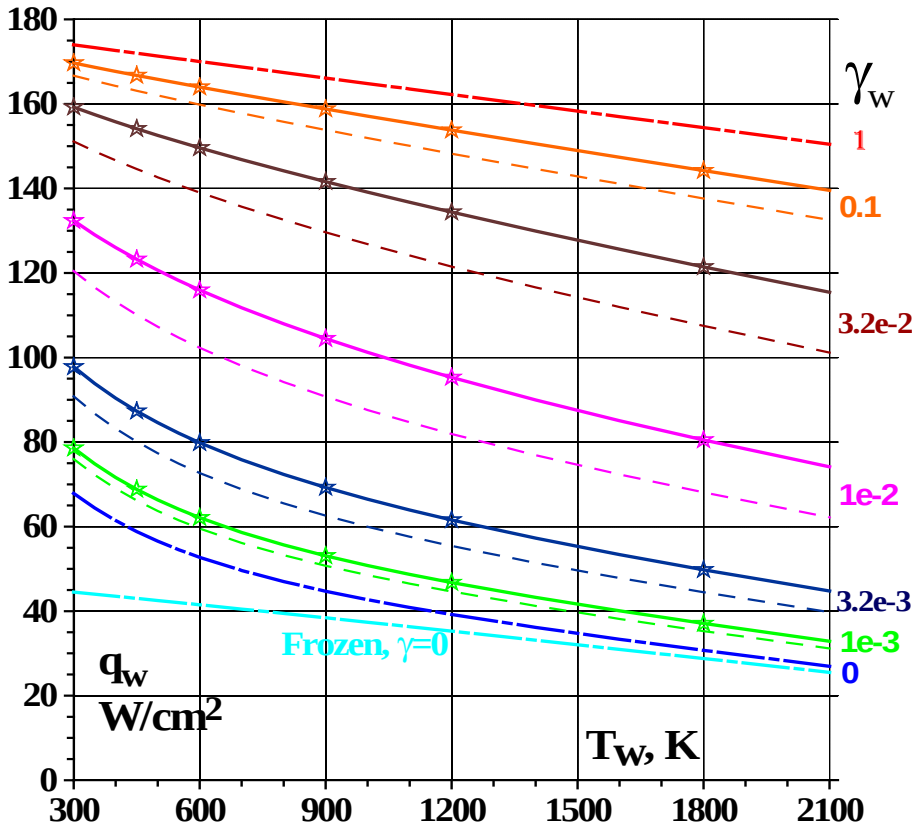

Figure 27: Heat flux envelopes for standard and novel surface catalysis models for extra regime: P=80 hPa, N_{ap}=45 kW, h_e=17.5 MJ/kg.

Alternative case of calculation by the novel model of surface recombination is presented below in Figs. 28-29. Here the two parameters γ_{wO} and γ_{wCO} are different. In fact, Figs. 28-29 present partial heat flux envelopes calculated by the novel model under the condition of fixed value of γ_{wCO} and variable γ_{wO} (Fig. 28), and fixed value of γ_{wO} and variable γ_{wCO} (Fig. 29). The dash curves in these figures show the ordinary heat flux envelopes calculated by the standard model with $\gamma_w = \gamma_{wO} = \gamma_{wCO}$. Both Figs. 28 and 29 are calculated for the test regime P=80 hPa, N_{ap}=40.4 kW, h_e=14 MJ/kg. Each figure consists of the two plots (a, b) with different values (1e-2 and 1e-3) of the fixed recombination coefficient for the novel model calculation.

Calculation results obtained by the novel model are presented in the limits of its application. In particular, the curve for γ_{wCO}=3.2e-2 is started at T_w=1100 K in Figs. 29 (a, b), because the novel model is not applicable at lower T_w.

Notations in Figs. 28-29:

solid black curves with colored stars - calculations by the novel model; variable recombination coefficient (γ_{wO} in Figs. 28 (a,b) and γ_{wCO} in Fig. 29 (a,b)) is shown to the right of corresponding curve outside the plot field;

dash colored curves are the results obtained by the standard model; values of γ_w are shown at corresponding curves in the field of plot;

the rest notations are the same as in Figs. 23-26.

It is clear from Figs. 28-29 that measured heat flux value to a testing material could be reproduced by Gamma computations in framework of the novel model with different pairs of (γ_{wO}, γ_{wCO}), i.e. the solution is not unique. To determine the unique solution, one can specify a fixed value of γ_{wO}, e.g. to use the appropriate literature data (if any).

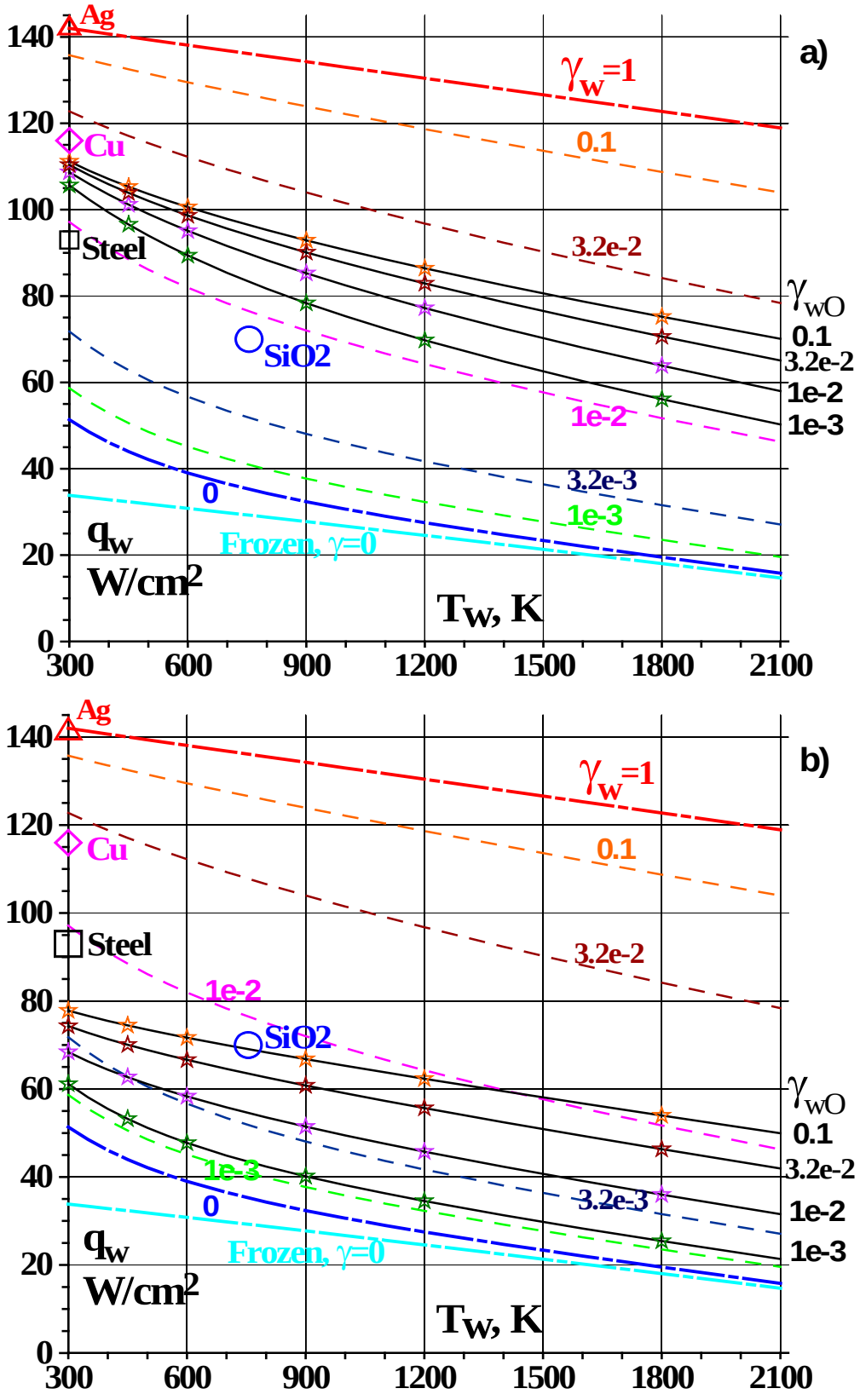

Figure 28: Heat flux envelopes for standard and novel catalysis models. Fixed γ_{wCO} =1e–2 (a) and 1e–3 (b) in the novel model.

Dash colored curves - standard model, $\gamma_w = \gamma_{wO} = \gamma_{wCO}$ is shown at the curves in the field of the plot. Black solid with stars - novel model with fixed γ_{wCO}. Variable γ_{wO} is shown to the right of curves. P=80 hPa, N_{ap}=40.4 kW, h_e=14 MJ/kg.

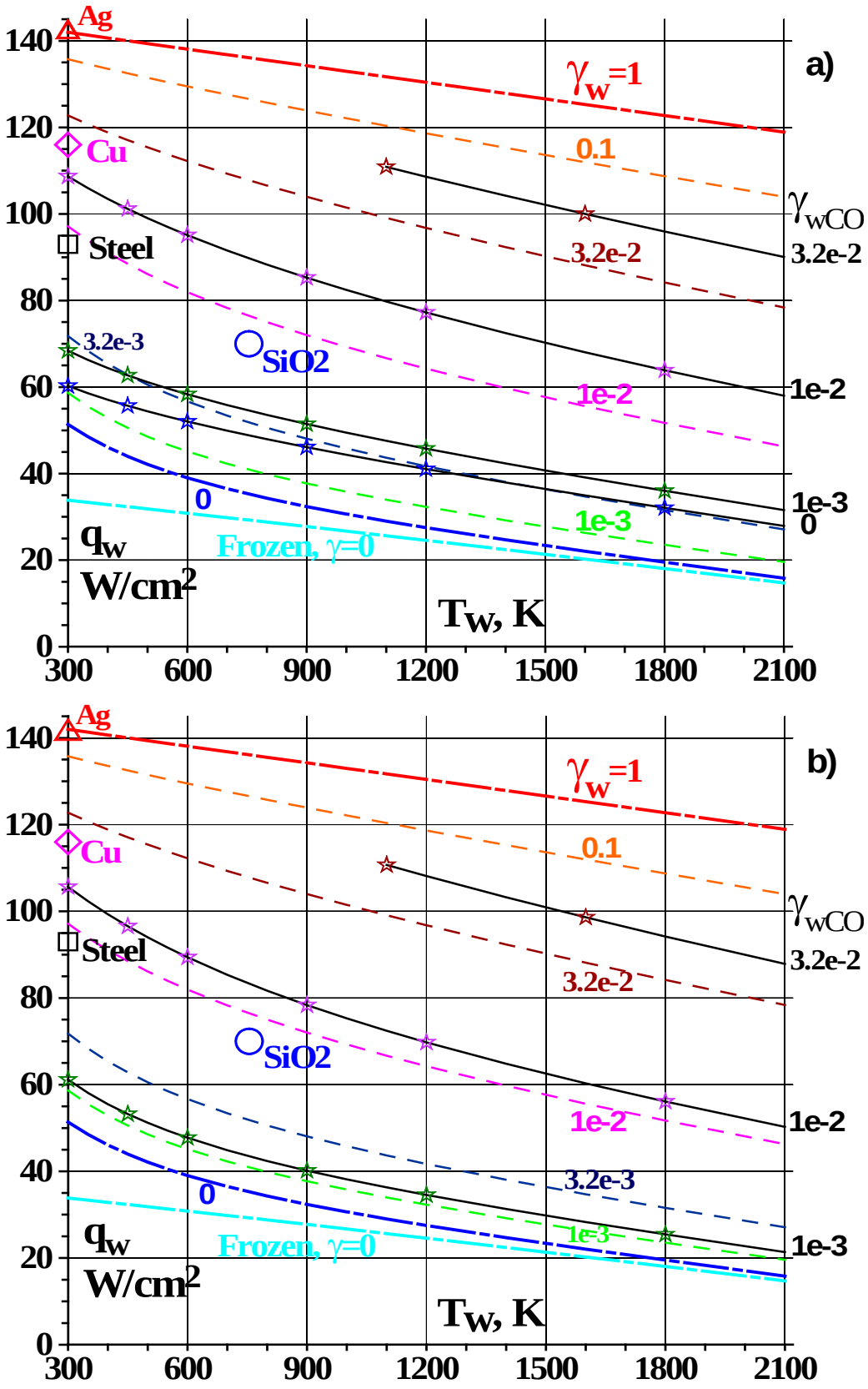

Figure 29: Heat flux envelopes for standard and novel catalysis models. Fixed γ_{wO} =1e–2 (a) and 1e–3 (b) in the novel model.

Dash colored curves - standard model, $\gamma_w = \gamma_{wO} = \gamma_{wCO}$ is shown at the curves in the field of the plot. Black solid with stars - novel model with fixed γ_{wO}. Variable γ_{wCO} is shown to the right of curves. P=80 hPa, N_{ap}=40.4 kW, h_e=14 MJ/kg.

To demonstrate capabilities of the novel model, we specify below oxygen recombination coefficient γ_{wO} according to literature data and determine CO recombination coefficient γ_{wCO} for the four test regimes for quartz and steel surfaces.

Value of γ_{wO} for quartz surface is assumed to be 2e-3 for all the test regimes, according to IPM previous data obtained in IPG-4 pure oxygen tests [37]. Analysis of literature data on γ_{wO} was presented in our previous report, see Fig. 17 in [34]. According to that analysis, γ_{wO} could vary from 2e-4 to 2e-2 for the surface temperature range T_w =500 - 1000 K, depending on experimental conditions, material and surface quality, and probably depending on experimental and theoretical uncertainties. The value of γ_{wO}=2e-3 is close to IPM data [37] obtained for pure oxygen flow at P=100 hPa, plasmatron power N_{ap}=45 kW, enthalpy h_e = 20 MJ/kg, and this value lays in the middle of the range of whole experimental data presented in Fig. 17 in [34].

Value of $\boldsymbol{\gamma_{wO}}$ for stainless steel is taken from [38]. In this work γ_{wO} = 2.6e-3 was obtained from the experiments in pure oxygen flow.

With use of the above mentioned fixed values of γ_{wO} for quartz and stainless steel surfaces, the second parameter γ_{wCO} is calculated by the novel model for the four test regimes. The results are presented in the Table 2. Value of γ_{wCO} is not determined for stainless steel for the single case P = 80 hPa, N_{ap} = 34 kW, T_w = 300 K, because for this case the novel model is not applicable at γ_{wO} = 2.6e-3, $\gamma_{wCO} \geq$ 7e-3 and the relatively high heat flux 66 W/cm^2 could not be reached in computations.

The determined values of γ_{wCO} are greater than γ_{wO} for both quartz and steel surfaces, with the exception of the single case P = 40 hPa, Zm=122 mm when $\gamma_{wO} = \gamma_{wCO}$ = 2e-3 for quartz.

To estimate the difference between catalycity parameters determined previously in [34] by the standard model and the newly determined parameters (γ_{wO}, γ_{wCO}), the last column in the Table 2 presents the old data for $\gamma_w = \gamma_{wO} = \gamma_{wCO}$ from [34]. It is clear that for all test regimes the newly determined parameters (γ_{wO}, γ_{wCO}) are lower than the appropriate effective catalycity parameter γ_w determined by the standard model, both for quartz and steel. However, the difference is not severe, the maximum ratio of γ_w to each of the two parameters (γ_{wO}, γ_{wCO}) is about factor of 4.

As a conclusion from this comparison, we can propose that the effective recombination coefficient γ_w calculated by the standard model provides the upper bound for catalycity parameters γ_{wO}, γ_{wCO} calculated by the novel model.

Table 2: CO surface recombination coefficient determined by the novel catalysis model.

P hPa	N_{ap} kW	Zm mm	testing material	T_w K	q_w W/cm^2	γ_{wO} specified by literature data	γ_{wCO} determined by novel model	$\gamma_w = \gamma_{wO} = \gamma_{wCO}$ determined previously by standard model
80	40.4	40	quartz	755	70	2e–3	6.0e-3	7.84e-3
			steel	300	93	2.6e–3	6.1e-3	8.48e-3
80	34.0	40	quartz	600	45	2e–3	3e-3	4.97e-3
			steel	300	66	2.6e–3	n/a	1.07e-2
40	35.0	72	quartz	606	46	2e–3	5e-3	5.71e-3
			steel	300	72	2.6e–3	9e-3	1.13e-2
40	35.0	122	quartz	500	30	2e–3	2e-3	3.42e-3
			steel	300	45	2.6e–3	7e-3	8.77e-3

7 Conclusions

Subsonic ICP flow parameters in IPG-4 segmented discharge channel with conical nozzle are calculated by Alpha code on the basis of Navier-Stokes and simplified Maxwell equations for the four IPG-4 test regimes realized for 97%CO_2+3%N_2 working gas according test matrix.

Parameters of 97%CO_2+3%N_2 equilibrium reacting subsonic jet flow over euromodel are calculated by Beta code on the basis of Navier-Stokes equations for the same IPG-4 test conditions.

The complete set of the dimensionless parameters is determined by Beta code computation results to be used as input data for Gamma code. These parameters characterize the boundary layer thickness, flow velocity and vorticity at the external edge of boundary layer in front of the testing model.

Numerical simulations of both ICP flow in discharge channel and subsonic jet flow over euromodel are performed for pure CO_2 working gas to compare with corresponding results obtained for 97%CO_2+3%N_2 flow. Comparison of the results revealed negligible influence of 3%N_2 addition on the main flow parameters and molar concentrations at the boundary layer external edge in front of the model.

One-dimensional 5-species (CO_2, O_2, CO, O, C) flow in nonequilibrium dissociated boundary layer with finite thickness near the model stagnation point was calculated by Gamma code to determine heat flux envelopes for the IPG-4 test regimes with CO_2 working gas. The calculations were made for the standard and the novel model of surface catalysis for O-atoms and CO-molecules recombination proposed in [34].

Numerical simulation revealed the limitation on the use of the novel model: input data for calculation (e.g. pressure, enthalpy, recombination coefficients γ_{wO}, γ_{wCO}) have to ensure sufficient concentration of oxygen atoms C_O in gas flow at the wall to provide the possibility of surface recombination for CO molecules defined by the corresponding recombination efficiency γ_{wCO}. When this condition is not provided, negative values of C_O appear in boundary layer computation to manifest inapplicability of the novel model for current regime and computation parameters (T_w, γ_w).

Comparison of calculations performed by the standard and the novel model of surface catalysis for the case $\gamma_{wO} = \gamma_{wCO} = \gamma_w$ shows that heat flux values q_w (T_w, γ_w) calculated by the novel model (within its application limits) are always higher than corresponding values calculated by the standard model. Consequently, values of the efficient recombination coefficient γ_w obtained with the novel model will be lower.

Partial heat flux envelopes are calculated by the novel model with different recombination coefficients γ_{wO} and γ_{wCO}, when one of the two coefficients is fixed, while the other is variable. For this two-parameter case, measured heat flux value to a testing material could be reproduced by Gamma computations with different pairs of (γ_{wO}, γ_{wCO}). To determine the unique solution, one can specify a fixed value for γ_{wO}, e.g. with use of appropriate literature data.

CO recombination coefficients γ_{wCO} are determined by the novel model for quartz and stainless steel for the four test regimes with use of the following fixed values of γ_{wO} taken from [37], [38]: γ_{wO} =2e-3 for quartz and γ_{wO} =2.6e-3 for steel. Comparison of the effective recombination coefficient $\gamma_w = \gamma_{wO} = \gamma_{wCO}$ obtained previously [34] by the standard model with the newly obtained catalytic efficiencies γ_{wO} and γ_{wCO} is presented. Value of γ_{wCO} is always lower (or equal) than the corresponding fixed value of γ_{wO}; both γ_{wO} and γ_{wCO} are lower than the corresponding effective recombination coefficient γ_w. So, the effective parameter γ_w provides probably the upper bound for the surface recombination coefficients γ_{wO} and γ_{wCO}.

8 References

[1] Vasil'evskii, S.A., Kolesnikov, A.F., Yakushin M.I.: *Determination of the Effective Probabilities of the Heterogeneous Recombination of Atoms When Heat Flow is Influenced by Gas-Phase Reactions*. High Temperature, Vol. 29, No. 3, 1991, pp.411-419 (Translated from Russian)

[2] Anfimov, N.A.: *TsNIIMASH capabilities for aerogasdynamical and thermal testing of hypersonic vehicles*. AIAA Paper 92-3962. 1992.

[3] Gordeev, A.N., Kolesnikov, A.F., and Yakushin, M.I.: *An Induction Plasma Application to "Buran's" Heat Protection Tiles Ground Tests*. SAMPE Journal, Vol. 28, No. 3, 1992, pp.29-33

[4] Laure, S., Auweter-Kurtz, M., Fasoulas, S., Kurtz, H.: *Reentry simulation within an induction heated plasma wind tunnel*. 2nd European Symposium on Aerothermodynamics for Space Vehicles, ESA SP-367, 1994, p.335

[5] Basele, J.M., Conte, D., Leroux, R.: *A new test facility for experimental characterization of high temperature composites and ceramics.* 3rd European Workshop on TPS. ESTEC, Noordwijk, The Netherlands, 25-27 March 1998.

[6] Vlasov, V.I., Zalogin, G.N., Lunev, V.V.: *Material Catalycity Effect on the Heat Transfer to Hypersonic Flight Vehicles in Multicomponent Gas Mixtures.* In: European Conf. on Aerospace Sci. (EUCASS). Moscow, 2005

[7] Kolesnikov, A.F., Gordeev, A.N., Vasilevsky, S.A.: *Simulation of Stagnation Point Heating and Predicting Surface Catalysity for the EXPERT Re-Entry Conditions*. Proceedings of the 6th European Symposium on Aerothermodynamics for Space Vehicles. ESA SP-659. 2009.

[8] Kolesnikov, A.F., Gordeev, A.N., Vasilevskii, S.A.: *Results of Experimental Study in the IPG-4 Facility*. SACOMAR. Del. No. D5.4. November 2011

[9] Vanden Abeele D., Vasil'evskii, S.A., Kolesnikov, A.F., Degrez, G., Bottin, B.: *Code-to-code validation of inductive plasma computations*. Progress in Plasma Processing of Materials. Eds. P.Fauchais and J.Amouroux, Begell House, N.Y., 1999. pp. 245-250

[10] Rini, P., Vasil'evskii, S.A., Kolesnikov, A.F., Chazot, O., Degrez, G.: *Inductively coupled CO_2 plasma flows: code-to-code comparison*. 4-th International Symposium Atmospheric Reentry Vehicles and Systems. 21-23 March, 2005, Arcachon, France. Published also in VKI RP 2005-57.

[11] Utyuzhnikov, S.V., Konyukhov, A.F., Vasil'evskii, S.A., Rudenko, D.V., Kolesnikov, A.F., Chazot, O.: *Simulation of sub- and supersonic flows in inductive plasmatrons*. AIAA Journal. Vol. 42, No. 9, 2004. pp.1871-1877

[12] Sakharov, V.I., Kolesnikov, A.F., Gordeev, A.N., Verant, J.-L.: *CFD modeling of thermally and chemically nonequilibrium flows in discharge channel in subsonic plasmatron jets of the flat-face model*. Proceedings of the 6th European Symposium on Aerothermodynamics for Space Vehicles. November 2008. Versailles, France. ESA SP-659.

[13] Bykova, N.G., Vasil'evskii, S.A., Pershin, I.S., Yakushin, M.I.: *Induction subsonic flows temperature measurements from atoms and molecule radiation*. E-MRS - IUMRS - ICEM Symposium. TPP-6 Thermal Plasma Processes. 30 May - 02 June 2000, Strasbourg, France

[14] Bykova, N.G., Vasil'evskii, S.A., Kolesnikov, A.F.: *The effect of radiation on the spatial distribution of the temperature of subsonic flows of induction plasma*. High Temperature. Vol. 42, No. 1, 2004, pp.12-19

[15] Vasil'evskii, S.A., Kolesnikov, A.F.: *Numerical modeling of flow in IPG-4 induction plasmatron. Comparison with experimental data and CFD calculations*. IPM RAS, Preprint No.953. Moscow, 2010. (In Russian)

[16] Rini, P., Vasil'evskii, S.A., Kolesnikov, A.F., Chazot, O., Degrez, G.: *CO_2 stagnation line flow simulation for Mars entry applications*. 38-th AIAA Thermophysics Conference, June 2005, Toronto, Canada. AIAA Paper 2005-5206. 11p

[17] Boulos, M.I.: *Flow and temperature fields in the fire-ball of an inductively coupled plasma*. IEEE Trans. on Plasma Sc. PS-4, 1976, Vol.1, p.28

[18] Vasil'evskii, S.A., Kolesnikov, A.F., Kubarev, S.N., Makarov, B.P., Yakushin, M.I.: *Nonequilibrium flow and heat transfer in induction plasma generators*. Heat Transfer Research. Vol.25, No.3, 1993, p.365

[19] Vasil'evskii, S.A., Kolesnikov, A.F., Yakushin, M.I.: *Mathematical models for plasma and gas flows in induction plasmatrons*. Molecular Physics and Hypersonic Flows. Edited by M.Capitelli. NATO ASI Series, Kluwer, Dordrecht. 1996, p.495

[20] Kolesnikov, A.F., Vasil'evskii, S.A.: *Some problems of numerical simulation of discharge electrodynamics in induction plasmatron*. Proceedings of 15th IMACS World Congress, Berlin, August 1997. Vol.3, Computational Physics, Chemistry and Biology. Ed. by A.Sydov. 1997, p.175

[21] Vanden Abeele, D., Degrez, G.: *Iterative methods for inductive plasma computations*. AIAA Paper 98 - 2825. 1998

[22] Patankar, S.V., Spalding, D.B.: *A calculation procedure for heat, mass and momentum transfer in three-dimensional parabolic flows*. International Journal of Heat and Mass Transfer. Vol.15, 1972, p.1787

[23] Patankar, S.: *Numerical heat transfer and fluid flow*. Hemisphere Publishing Corp. N.Y. 1980.

[24] Vasil'evskii, S.A., Kolesnikov, A.F.: *Multiparameter investigation of flow in the induction plasmatron and subsonic exhaust jet*. Up-to-date Problems in Mechanics. Phisico-chemical mechanics of fluids and gases. Proceedings of the IPMech RAS. Moscow, Nauka Publ. 2010. pp.178-200 (In Russian).

[25] Vasil'evskii, S.A., Sokolova, I.A., and Tirskii, G.A.: *Exact equations and transport coefficients for a multicomponent gas mixture with a partially ionized plasma*. Journal of Applied Mechanics and Technical Physics. Vol. 25, No.4, 1984. pp. 510-519 (Translated from Russian)

[26] Gurvich at al.: *Thermodynamic properties of individual substances*. In 4 volumes. Ed. Glushko V.P. Moscow, Nauka Publ. 1979-1982 (In Russian)

[27] Vasil'evskii, S.A., Sokolova, I.A., and Tirskii, G.A.: *Definition and computation of effective transport coefficients for chemical-equilibrium flows of partially dissociated and ionized gas mixtures*. Journal of Applied Mechanics and Technical Physics. Vol. 27, No.1, 1986. pp. 61-71 (Translated from Russian)

[28] Kolesnikov A.F, Tirskiy G.A.: *Equations of hydrodynamics for partially ionized multicomponent mixtures of gases, employing higher approximations of transport transfer coefficients*. Fluid Mechanics - Soviet Research, Scripta Technica Publ., Vol.13, No.4, 1984, pp.70–97. (Translated from Russian collected papers "Molecular Gasdynamics" issued by Nauka Publ. in 1982)

[29] Devoto, R.S.: *Transport properties of ionized monoatomic gases*. Physics of Fluids, 1966, v.9, N.6, pp.1230-1240

[30] Ferziger, J.H., Kaper, H.G.: *Mathematical theory of transport processes in gases*. Amsterdam-London. North-Holland publishing company (1972)

[31] Sokolova, I.A.: *Computer library of transport properties for atmosphere gases and plasma.* Mathematical Modeling. Vol.10, No.2, 1998, pp.25-40 (translated from Russian)

[32] Kolesnikov, A.F., Pershin, I.S., Vasil'evskii, S.A., and Yakushin, M.I.: *Study of Quartz Surface Catalycity in Dissociated Carbon Dioxide Subsonic Flows*, Journal of Spacecraft and Rockets, Vol. 37, No. 5, pp573-579

[33] Park, C., Howe, J. T., Jaffe, R. L., and Candler, G. V.: *Review of Chemical-Kinetic Problems of Future NASA Missions, II: Mars Entries*, Journal of Thermophysics and Heat Transfer, Vol.8, No.1, 1996, pp.9–23.

[34] Kolesnikov, A., Vasilevskii, S., Levitin A., Gordeev, A.: *Report and library on surface chemistry*. SACOMAR. Del. No. D6.4. January 2012

[35] Kovalev, V.L.: *Heterogeneous Catalytic Processes in Aerothermodynamics*. Moscow: Physmatlit Publ., 2002 (in Russian)

[36] Petukhov, I.V.: *Numerical solution of two-dimensional boundary layer flows*. Numerical methods for solution of differential and integral equations and quadrature formulas. Addendum to Journal of Computational Mathematics and Mathematical Physics. Moscow, Nauka. Vol.4, No.4, 1964, pp.304-325. (in Russian)

[37] Kolesnikov, A., Yakushin, M., Vasil'evskii, S., Pershin, I., Gordeev, A.: *Catalysis effects on quartz surface in high-enthalpy subsonic oxygen & carbon dioxide flows*. Proceedings of the 3-d European Symposium on Aerothermodynamics for Space Vehicles, Noordwijk, 1998. ESA SP 426, pp.537-544.

[38] Cauquot, P., Cavadias, S., Amouroux, J.: *Thermal Energy Accommodation from Oxygen Atoms Recombination on Metallic Surfaces*. Journal of Thermophysics and Heat Transfer. 1998, Vol.12, No.2, pp.206-213.